JGR Planets

Key Points:
- Young craters are characterized by high roughness, rock abundance, soil temperature; these parameters decrease toward equilibrium with age
- Continuous ejecta reach roughness equilibrium faster than other subunits; small craters located in the maria form more rocks
- Unusual young regolith flows in Late Imbrian crater Bonpland D are interpreted to be caused by a recent strong shallow seismic event

Supporting Information:
- Supporting Information S1

Correspondence to:
J. Liu,
liujianzhong@mail.gyig.ac.cn

Quantitative Characterization of Impact Crater Materials on the Moon: Changes in Topographic Roughness and Thermophysical Properties With Age

Juntao Wang[1,2,3] ID, Mikhail A. Kreslavsky[3] ID, Jianzhong Liu[1,4,5] ID, James W. Head[6] ID, Ke Zhang[1,2], Maria M. Kolenkina[7], and Li Zhang[1]

[1]Center for Lunar and Planetary Science, Institute of Geochemistry, Chinese Academy of Sciences, Guiyang, China, [2]University of Chinese Academy of Sciences, Beijing, China, [3]Earth and Planetary Sciences, University of California, Santa Cruz, CA, USA, [4]Center for Excellence in comparative planetology, Chinese Academy of Sciences, Hefei, China, [5]Now at Institute of Geochemistry, Chinese Academy of Sciences, Guiyang, China, [6]Earth, Environmental, and Planetary Sciences, Brown University, Providence, RI, USA, [7]MExLAB, Moscow State University of Geodesy and Cartography (MIIGAiK), Moscow, Russia

Abstract Impact craters are the dominant features on the Moon, and their degradation with time is the most common geological process on this body. This work is aimed at detailed quantitative characterization of this process. We quantitatively characterize crater materials by (1) the topographic roughness calculated from Lunar Orbiter Laser Altimeter and (2) rock abundances and nighttime soil temperatures derived from Diviner measurements. In contrast to preceding works, we separately consider crater material subunits: central peaks, floors, walls, and continuous ejecta to study their degradation in detail. We mapped totally 4,770 individual crater material subunits. All subunits of the youngest craters are characterized by increased roughness, rock abundance, and soil temperature. These parameters decrease with age and tend toward equilibrium, stable state; the continuous ejecta reach equilibrium more rapidly than other subunits. Kilometer-baseline roughness of crater walls in the lunar maria is higher than in the highlands. Rock abundances and soil temperatures of the walls and floors of simple craters in the maria are also higher than in the highlands. We attribute these trends to differences in the mechanical properties of the target materials. Although the properties studied are not exact proxies for age, they can be used to assess individual age predictions; for example, several craters that were erroneously classified as Copernican have been detected. We also found that the unusual thermophysical signature of the walls of the Late Imbrian crater Bonpland D is due to recent regolith flows that could have been caused by a strong, shallow seismic event.

Plain Language Summary Impact craters have been forming on the Moon by meteoritic impacts throughout billions of years of its history. To assess their changes with time (degradation), we mapped many such craters in detail and studied their quantitative characteristics using data from the Lunar Reconnaissance Orbiter. In particular, we used data characterizing surface topography and rockiness. We found that the youngest craters are the roughest and the rockiest. With age, craters become smoother and rocks disappear. This happens for all parts of the craters; these changes occur more rapidly, however, for the area around the craters covered with material excavated by the impact. We found several craters that had been marked as very young on older geological maps of the Moon but are very smooth and lack rocks; we believe that they were misclassified. We also found one moderately old, but extremely rocky crater. In zoomed-in images we found very fresh, unusual landslides on its slopes; we suggest that these landslides were caused by strong, geologically recent moonquakes.

1. Introduction

Meteoritic impacts are the main exogenic process occurring throughout the evolution of the Moon, and impact craters are the dominant landforms on the lunar surface (Melosh, 1989; Wilhelms et al., 1987). Crater studies are important in planetary science. Crater size-frequency distribution measurements are powerful tools in the dating of planetary surfaces (Neukum et al., 2001); in addition, crater degradation is widely used in age dating (Craddock & Howard, 2000; Fassett & Thomson, 2014; Head, 1975). Impact

craters act as useful tools for studies of the properties of the surface and near subsurface, and the formation of related landforms on the Moon (Cintala et al., 1977; Wood et al., 1977). Furthermore, materials ejected from large craters or impact basins act like sedimentary strata, which can be used as stratigraphic markers to build the lunar stratigraphic column (Wilhelms et al., 1987). Therefore, crater materials play an important role in lunar geologic mapping and reconstruction of lunar history.

Material associated with impact cratering events can be divided into crater floor, walls, and rim subunits (Wilhelms, 1970). In the framework of the 1:5,000,000 scale geological mapping program by U.S. Geological Survey (USGS) in the 1970s (Lucchitta, 1978; McCauley & Wilhelms, 1971; Scott et al., 1977; Wilhelms & El-Baz, 1977), however, investigators usually mapped the crater materials in their entirety, which was due to the limitations of image resolution and the scale of the geological maps. Crater material subunits were partly drawn only on some larger scale, regional geological maps (Hackman, 1962; Scott, 1972). The recent 1:5,000,000 scale unified global lunar geologic maps (Fortezzo et al., 2020) continue to combine these subunits. In the frame of ongoing Chinese 1:2,500,000 global lunar geologic mapping project (Liu et al., 2016, 2017), the crater materials are subdivided into central peak, floor, wall, continuous ejecta, and rays. Dividing and comparing the crater material subunits enables more detailed studies of the characteristics of the different crater materials and their regional and temporal variations. Each specific unit of crater material has been independently studied in many aspects. For example, the maturity of impact crater rays as the criterion of distinguishing between Copernican and Eratosthenian age (Grier et al., 2001; Hawke et al., 2004; Werner & Medvedev, 2010), impact melt volume and distribution (Bray et al., 2010; Cintala & Grieve, 1998; Dhingra et al., 2017), ejecta deposition and emplacement (Guo et al., 2018; Jones et al., 2016; Luther et al., 2019), and central peak morphology and mineralogy (Hale & Head, 1979; Lemelin et al., 2015). Less attention has been paid to the difference between degradation processes affecting the various subunits of crater materials; a topic would be very useful in order to better understand impact crater formation and degradation processes.

Craters undergo degradation with age: The sharp morphology of pristine craters becomes subdued due to smaller impacts, mass wasting, lava flooding, and proximity weathering from larger impact events. Head (1975) divided lunar crater degradation into two time periods based on different styles and rates of crater degradation processes. Period I, prior to about 3.85–3.95 Ga ago, is characterized by a high influx rate and by the formation of large, multiringed basins. Period II, from about 3.85–3.95 Ga to present, is characterized by (1) a much lower influx rate and (2) lack of large multiringed basins. In contrast, craters formed throughout Period II show more subtle changes in morphologic characteristics with time.

Many researchers have studied crater degradation with age; however, they typically focused on the morphometric characteristics (such as the ratio of depth to diameter and subjective features such as the sharpness of the crater rim crest) and also typically considered each crater as a whole (Agarwal et al., 2019; Fassett & Thomson, 2014; Mahanti et al., 2018; Pike, 1977a). Ghent et al. (2014) studied the disappearance of rocks in crater ejecta with age, which has important implications for estimating the ages of young craters (Mazrouei et al., 2019). Characteristics of impact crater materials also vary with target substrate and crater size. The studies of target substrate effects, however, were mostly focused on the crater and ejecta formation (Cintala & Grieve, 1998; Dundas et al., 2010; Luther et al., 2018; Osinski et al., 2019; Richardson, 2009) rather than on their postimpact modification with time. Crater and ejecta morphology is closely related to crater size (Florensky et al., 1976; Melosh, 1989). In this study we explore quantitatively the different subunits of crater materials to better understand (1) how they change (degrade) with time, (2) how the target material affects this process, and (3) how the crater size influences these trends. Although craters have been previously discussed with respect to these factors, research usually focused on entire craters or only on a single part of crater material, for example, ejecta or rays. We focus on the detailed comparison of effects of time, crater size, and nature the substrate on the several different crater material subunits in order to learn more about crater degradation processes on the Moon.

The Lunar Reconnaissance Orbiter (LRO) has now provided high-resolution images, topographic data, and thermal-infrared measurements (Chin et al., 2007; Paige et al., 2010; Robinson et al., 2010; Smith et al., 2009). Accurate quantitative characterization of each crater material subunit is now possible and more practical using these new data sets. We can also obtain more quantitative attributes of craters and their degradation, such as topographic roughness, nighttime regolith temperature, and rock abundance
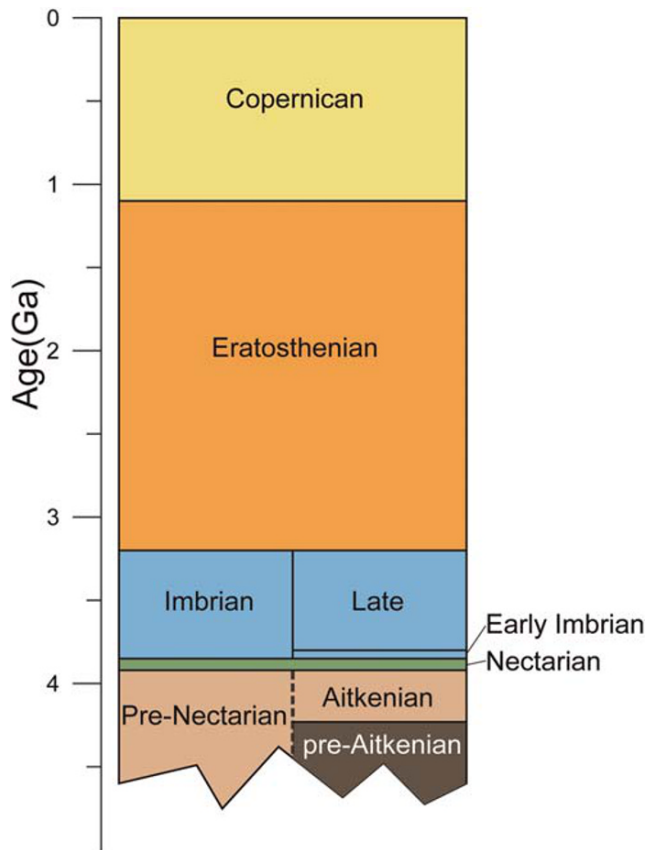
Figure 1. The geologic time scale of the Moon. Absolute ages corresponding to the periods and epochs are shown according to Stöffler et al. (2006).

(Bandfield et al., 2011; Kreslavsky et al., 2013). In this study, through those several quantitative measurements, we characterize the crater material subunits and analyzed the diversity of crater material subunit properties with respect to stratigraphic age, location, and crater size. Based on our results, two additional implications are described for certain craters: (1) reclassification of crater stratigraphic age and (2) identification of older craters characterized by recent active processes.

The paper is organized in the following way. In the next section, we describe the data we used and explain the calculation of the quantitative measures that characterize crater subunits. Section 3–5 treat degradation with stratigraphic age, the effect of substrate material, and the influence of crater size, respectively. In section 6 we describe the implications for stratigraphic age identification and assessment of unusual craters.

2. Data and Method

2.1. Crater Database

We used the LPI lunar crater database (Losiak et al., 2009), which is reviewed and updated continuously. Specifically, we used the 2015 version (https://www.lpi.usra.edu/scientific-databases/), the most recent version at the time of writing. The database contains information from several previous studies of lunar craters, including abundant and detailed attributes for 8,716 craters, with stratigraphic ages for 1,675 of them. The stratigraphic age is defined in terms of six main subdivisions (Wilhelms et al., 1987): the Pre-Nectarian Period, Nectarian Period, Early Imbrian Epoch, Late Imbrian Epoch, Eratosthenian Period, and Copernican Period. Liu and Guo (2018) and Guo, Ji, et al. (2016) have used the term Aitkenian Period for a part of the Pre-Nectarian postdating the South Pole-Aitken basin-forming impact (Figure 1); we follow this terminology in the present paper. We chose this database, rather than the Robbins (2019) database because it has designations of stratigraphic age

for craters. Larger impact basins whose diameters are larger than 200–300 km (Baker et al., 2017; Neumann et al., 2015; Wilhelms et al., 1987) are much more complex and their formation and modification processes differ from those of smaller simple and complex craters; therefore, we focus on the 1,491 craters with known stratigraphic age, diameters less than 200 km, and units that are not overlapped completely by other ejecta. The smallest craters studied are ~2 km in diameter. The database is not exhaustive: While it lists the majority of the largest young (Copernican and Eratosthenian) craters, the older and smaller crater lists are incomplete. Therefore, the database is not suitable for the study of size-frequency distributions.

Utilizing the selected crater database (Losiak et al., 2009), crater material subunits for each crater were mapped on the basis of images and topographic data from the LRO mission. This mapping work is a part of the Chinese lunar geologic mapping project at the scale of 1:2,500,000 (Liu et al., 2016), a larger effort that is progressing successfully. We subdivide materials for each crater into five subunits (Liu et al., 2016, 2017): central peak material (CP), floor material (CF), wall material (CW), continuous ejecta (CE, also called "crater rim material"), and rays (discontinuous ejecta, also called "radial material"). Rays are mapped only for the youngest (Copernican age) craters, on the basis of their well-known degradation and loss in craters older than Copernican age (e.g., Wilhelms et al., 1987). Technically, our approach is to manually draw a polygonal outline in ArcGIS around the geological subunits of each crater using image mosaics and topographic data as base maps; an example is shown in Figure 2. In total, we mapped 4,770 subunits for 1,491 craters. Locations of mapped craters are shown in Figure 3 and the mapped subunits are illustrated in supporting information Figure S1.

2.2. Terrain Types

It is reasonable to expect that the characteristics of the impact crater subunits depend on the nature of the target material and other geological factors. On the Moon (Wilhelms et al., 1987), there is a prominent
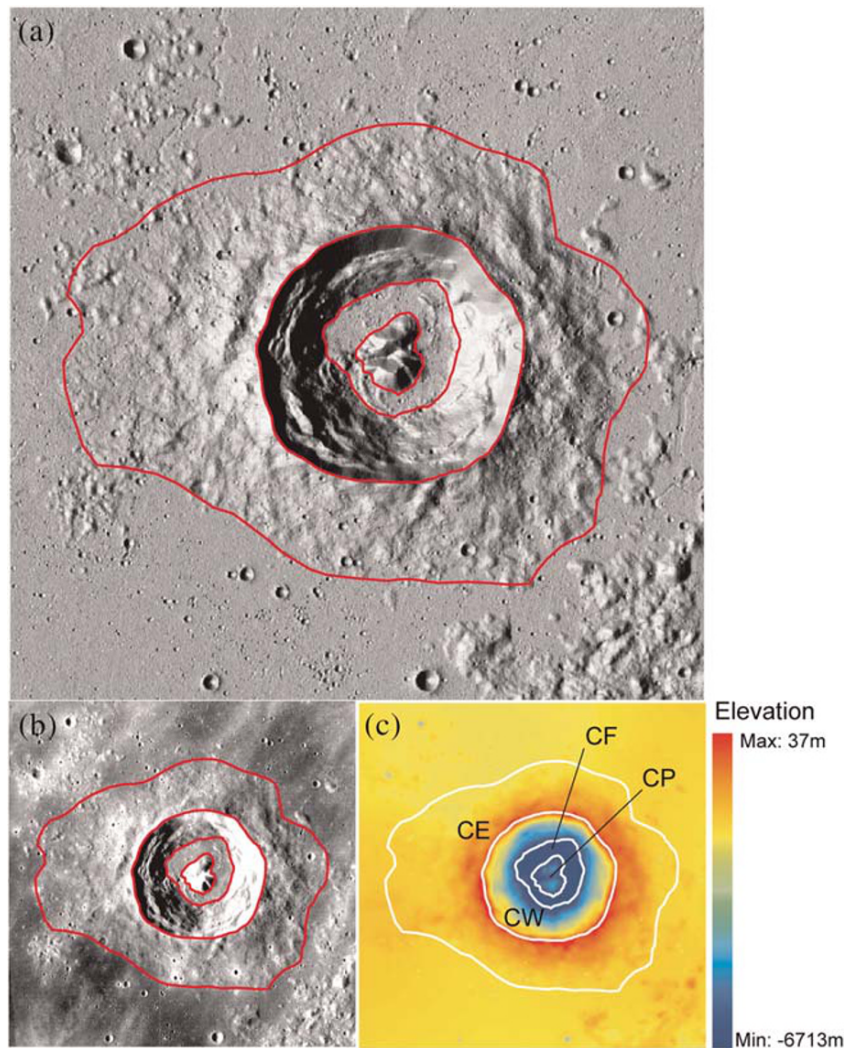
Figure 2. Example of subdivision and mapping of crater material subunits. Crater Lansberg is centered at 0.31°N, 26.63°W; its diameter is 38.8 km. Red and white lines are outlines of each subunit; from inside the crater outward, central peak (CP), crater floor (CF), crater walls (CW), and continuous ejecta (CE). (a) Artificial hill-shade image from digital elevation model SLDEM2015 (Barker et al., 2016), which was derived from Kaguya Terrain Camera stereo images and Lunar Orbiter Laser Altimeter (LOLA) data. (b) LROC (Lunar Reconnaissance Orbiter Camera) Wide Angle Camera (WAC) image mosaic. (c) Digital elevation model (DEM) map from LOLA data.

dichotomy of target material between mare and highland terrain: highland target material is predominantly old, likely primordial crust with a thick megaregolith layer (Hartmann, 2003; Short & Forman, 1972) reworked by old impacts, while the maria are volcanic plains of mafic composition that have not been significantly reworked by large impacts. This underlines the broad age range difference between the two dichotomous terrains. It is natural to analyze the differences between craters formed in maria and highlands. However, the subdivision of craters into those in the mare and highland materials is often difficult and not straightforward. A number of larger craters are superposed on the mare/highland boundary, and attribution to either terrain is ambiguous. It would be natural to assign all craters predating mare formation to the highlands. The fact that a crater is embayed by mare material, however, means only that the crater predates the last local episode of lava emplacement; it does not necessarily mean that the crater predates the mare itself, and attribution of embayed craters to either terrain can also be ambiguous. We partly mitigated this problem by creating a generalized outline of mare terrain (Figure 3), which was drawn manually on the basis of the detailed mare outline of Nelson et al. (2014). Small mare patches were excluded, small highland "islands" were included in maria, and the boundaries
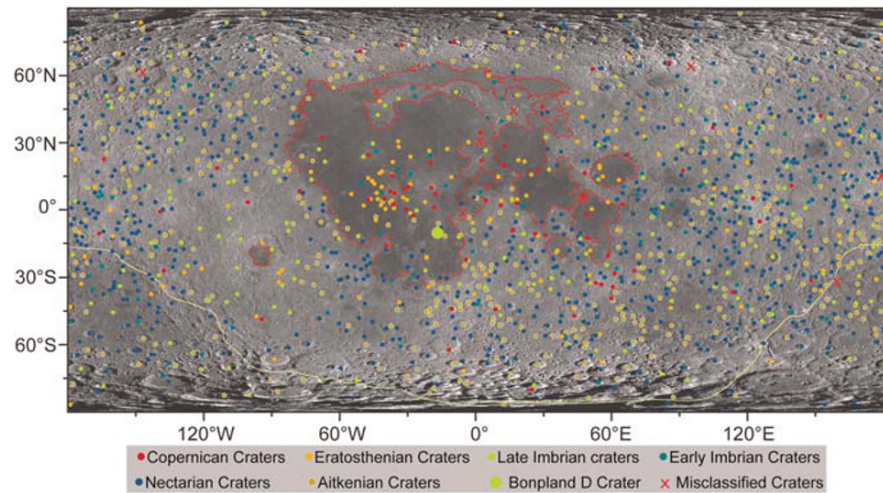
Figure 3. Generalized outlines of maria (red outline) and SPA terrain (yellow outline) adopted in this analysis. Colored dots show all craters from the LPI database (Losiak et al., 2009), with the color indicating stratigraphic age according to that database. Specifically marked are misclassified craters (section 6.1) and the crater Bonpland D (section 6.2). The base map is the global LROC WAC image mosaic. Simple cylindrical projection centered at the nearside center.

of large mare expanses remained unchanged. We attributed craters with their centers within this generalized outline to the maria and all others to the highlands. This correctly placed old craters with volcanic infill on their floors into the highlands. It also correctly placed craters overlapping the mare/highland boundary into maria or highlands, depending on where a larger part of the crater is located. Although the attribution of a specific individual crater may in some cases still be ambiguous, our approach provides a simple and reasonable approximation and provides a basis for the detection of meaningful statistical trends.

On the basis of global geochemistry, Jolliff et al. (2000) subdivided the lunar crust into three major terranes: the Procellarum KREEP terrane, the Feldspathic Highlands terrane, and the South Pole-Aitken (SPA) terrane. Other authors subdivided the lunar surface on the basis of typical geophysical and topographic characteristics, obtaining three regional units with slightly different outlines (Guo, Liu, et al., 2016; Liu & Ji, 2018; Wieczorek et al., 2013). The SPA basin was one of those units. In this paper, we also subdivided terrains outside the generalized mare outline into typical highland terrain and SPA terrain, outlining the SPA terrain along the edge of the topographically low SPA basin (Figure 3). Highland terrain is characterized by moderate and high elevations, thick crust, and felsic composition with low amounts of iron. SPA terrain has the lowest elevation, thin crust, and a higher iron abundance.

2.3. LOLA Data and Roughness: The Interquartile Range of Profile Curvature

We use topographic data obtained by the Lunar Orbiter Laser Altimeter (LOLA) onboard the LRO (Smith et al., 2010) to calculate topographic roughness. The unprecedented ranging precision of LOLA along-orbit-track profiles, which are available from the National Aeronautics and Space Administration (NASA) Planetary Data System (PDS), enables robust characterization of terrains through topographic roughness. Each LOLA laser shot is used to obtain the range to five spots on the surface; in this work, we use only spot #3, which has the greatest number of valid measurements (Smith et al., 2009). We use data only from the nearly circular orbit.

There are a number of methods of calculating topographic roughness from topographic profiles (Bandfield et al., 2015; Helfenstein & Shepard, 1999; Kreslavsky et al., 2013; Rosenburg et al., 2011; Shepard et al., 2001). In this paper, we apply the "interquartile range of profile curvature", the advantages of which have been discussed in (Kreslavsky et al., 2013). In addition, its application to different subunits of crater materials has been shown by Kreslavsky et al. (2013) (Figures 9 and 13 in that paper); they also showed the usefulness of hectometer and kilometer scale roughness for researching small and large craters, and even impact basins. Roughness depends on the baseline length L, which can be considered as a measure of the characteristic spatial scale. This dependence bears essential information, as we will show in detail in later sections. In Figure 4, we can see how the different baselines used for roughness calculation are compared to typical
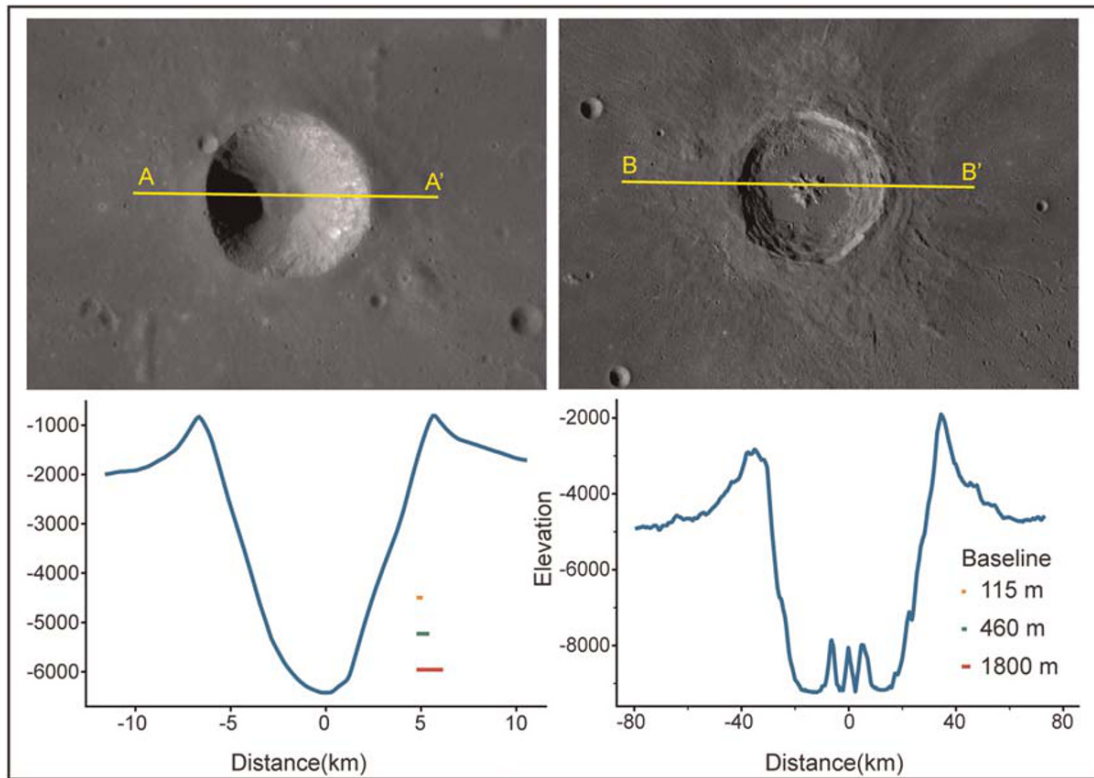
Figure 4. Images and topographic profiles of typical simple (left) and complex (right) craters. Short horizontal color bars show the baselines used for characterization of topographic roughness. Left, crater Milichius, $D = 13$ km. Right, crater Aristillus, $D = 55$ km.

profiles of smaller and larger craters. The minimal baseline is the double of ~57.4 m separation between consecutive data points along the orbit track, which means $L = 115$ m. The minimal baseline used by Rosenburg et al. (2011) is 17 m; however, the precision of LOLA data for baselines shorter than shot-to-shot distance is slightly affected by the so-called LOLA anomaly (Smith et al., 2010). This might cause some (minor) biases in the shortest possible baseline data. Therefore, we decided to limit ourselves to the shot-to-shot distance to be sure that the data are as accurate as possible. In addition to this shortest baseline, we also calculate roughness at the baselines of 4, 8, 16, and 32 steps, which is $L = 230, 460, 920,$ and 1.8 km. For each material subunit of each selected crater, we calculate all curvature values c of each data point located within the subunit by the formula:

$$c = \frac{Z_{2/L} + Z_{-2/L} - 2Z_0}{L^2},$$

where $Z_{2/L}$, $Z_{-2/L}$, and Z_0 are the elevation values half-a-baseline ahead, half-a-baseline behind, and at the given data point. After we obtained all curvature values for each LOLA profile within a given subunit, we calculated the quartiles $c_{1/4}$, $c_{3/4}$ of this subunit's curvature distribution. Then the roughness value is calculated as the interquartile range by the equation below:

$$r = c_{3/4} - c_{1/4}.$$

The roughness values of each crater material subunit for each baseline are stored as crater attributes. Supporting information Table S1 contains calculated roughness values for each subunit.

2.4. Thermophysical Properties

The Diviner radiometer onboard LRO provides thermal infrared measurements that are used to study the thermophysical properties of the lunar surface. Multiband spectral measurements indicate that the
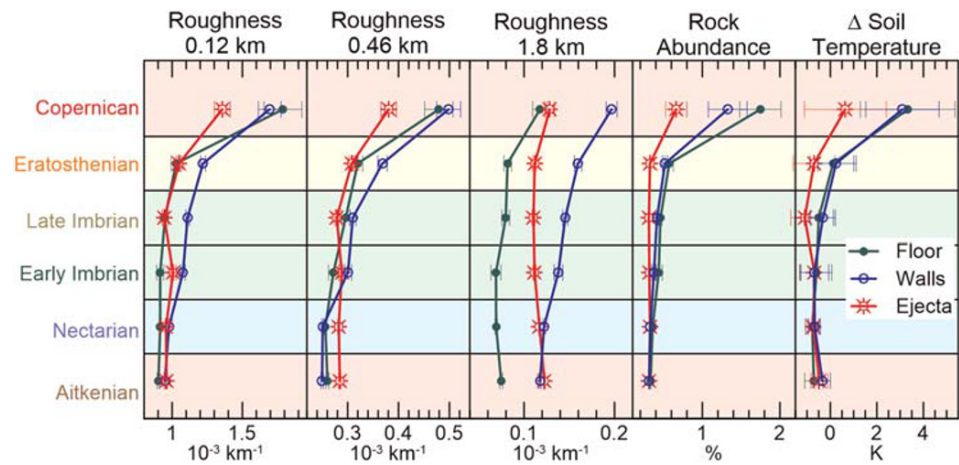
Figure 5. Roughness, rock abundance, and soil temperature as functions of stratigraphic age, plotted against the vertical axis in stratigraphic order (the most recent on top, from Copernican to Aitkenian). Only the 115, 460, and 1.8 km baselines are shown for topographic roughness. Error bars represent standard errors.

surface temperature within the radiometer resolution element is not uniform. Bandfield et al. (2011) modeled nighttime thermal emission with a two-component regolith model consisting of warmer rocks and colder soil. Fitting the model to the data resulted in two data sets: (1) the nighttime soil temperature and (2) rock abundance. The mean values of rock abundance are 0.4–0.5% and 0.4%–0.6% for highland and mare terrains, respectively (Ghent et al., 2014). Although high rock abundance often correlates with coarse soil, and, therefore, with a higher nighttime soil temperature, these derived parameters are not one-to-one correlated with each other and represent essentially different characteristics of the lunar regolith (Bandfield et al., 2011). For rock abundance, we use the average rock abundance map version with improvements accounting for local slopes described by Bandfield et al. (2016). For the soil temperature, we use the average soil-temperature map, which has been normalized by subtracting latitude trends (Bandfield et al., 2011). We refer to these data as "soil temperature" hereafter for brevity. It is not, however, an actual temperature, but a deflection of the derived nighttime temperature from the global latitudinal trend. Both data sets are available from the PDS. The maps that we use are plotted in simple cylindrical projection, extend from 80°N to 80°S latitude, and are sampled at 128 pixels per degree.

We used custom-coded Python scripts to calculate a single property value for each crater material subunit. We calculated the mean values of all map pixels within each subunit for rock abundance and the median value for soil-temperature. The median provides a robust measure of a typical parameter value within each subunit; however, small median values of rock abundance are blemished by the coarse quantization of rock abundance in the source data set. The value of rock abundance is the areal fraction of the surface covered by rock fragments represented in the released data set with an accuracy of one decimal place in percentage, which results in discrete median values. Therefore, we adopt the mean as a measure of typical rock abundance.

In analyzing the soil-temperature measurements for the subunits, we found a minor but conspicuous latitudinal trend (supporting information Figure S2). Since the soil-temperature data should have the latitudinal trend subtracted, we further compensated for this by subtracting the fitting value, which we approximated with a symmetric quadratic polynomial function of latitude (supporting information Figure S2). Supporting information Table S1 contains both the originally retrieved and renormalized soil-temperature values for each subunit, as well as the retrieved mean rock abundance values.

3. Degradation of Crater Material With Age

In this section, we describe the degradation of crater material with age through the assessment of the quantitative attributes of the units. Impact craters can be divided into simple and complex categories on the basis of their morphology. The typical crater transition diameter for the Moon has been discussed in many studies
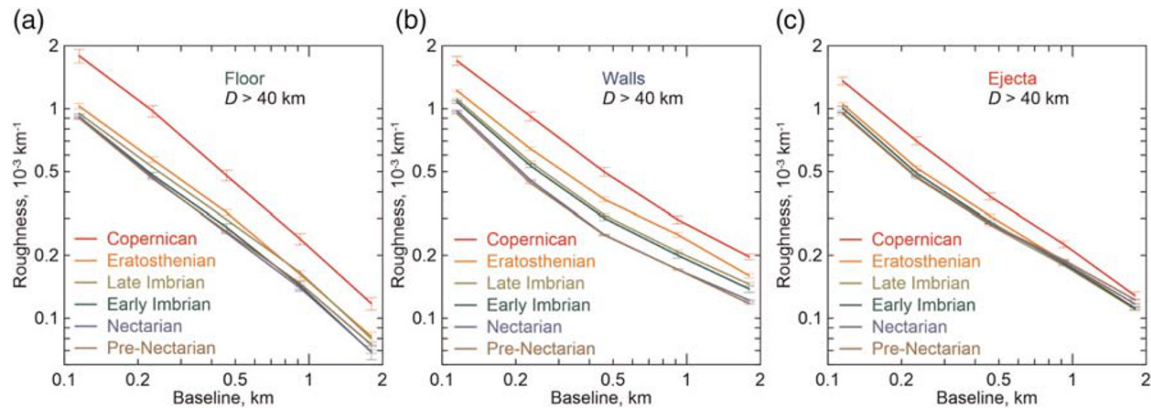
Figure 6. Median topographic roughness as a function of baseline for each stratigraphic age. Each pane refers to the specific subunit: (a) crater floor, (b) crater wall, and (c) continuous ejecta. The lines connect data points that represent the median topographic roughness at a given baseline calculated over given subunits of all craters belonging to the indicated stratigraphic age. The baselines were described in section 2.3. The scales of the horizontal and vertical axes are logarithmic. Error bars represent standard errors.

(Kalynn et al., 2013; Krüger et al., 2018; Pike, 1977a, 1977b), and here we utilize the transition from transitional craters to complex craters, for the fresh young crater, at diameters of ~28 km (highland) and ~24 km (mare) from Krüger et al. (2018). We also note that, relative to younger ones, older, simple craters are underrepresented in the database. Therefore, we summarize age trends only for craters larger than 40 km, which is larger than the fresh crater transition diameter, to eliminate any size-induced biases, thus excluding all simple and transitional craters to avoid the differences among simple and complex craters. The effects of crater size are further discussed in section 5.

3.1. Topographic Roughness

The median roughness values calculated for subsets of craters represent typical values for those subunits belonging to a given stratigraphic age. The comparison among subunits is shown in Figure 5. The roughness trend with age at various baselines can also be seen in Figure 6. Figure 7 illustrates the subunit textures.

Typically, roughness always declines with age for all baselines (Figures 5 and 6). We interpret this as being due to progressive degradation of craters by a number of processes: (1) disintegration of rocky materials by smaller impacts (e.g., Basilevsky et al., 2013); (2) formation of regolith and its transport to local lows (e.g., Heiken et al., 1991); (3) burial of rough topography by smoother ejecta from nearby craters (proximity weathering) (e.g., Head, 1975); and (4) burial of rough topography by smooth lavas (e.g., Whitten & Head, 2013).

Although all plots (Figures 5 and 6) show a general decrease in roughness with age, there are interesting variations. If we focus on the Copernican craters, we see that the roughness of CF (floors) is similar to or a little greater than CW (walls) at the shorter (hundred[s] of meters) baseline; however, the situation reverses at longer (kilometer[s]) baselines. The high-resolution images show that relatively fresh solidified impact melt, which covers crater floors, has a rough texture with large blocks, cracks, etc. (the "primary crater floor roughness" of Head, 1975). Features of that scale (tens of meters) contribute significantly to the roughness at the shortest baseline (Figures 7d and 8), but their contribution disappears at long baselines, over which melt is essentially flat. Crater walls (CW) typically do not display such extensive features (Figures 7e and 8). On the other hand, the long-baseline roughness of the crater walls is inherently higher due to the steep topographic signature of the crater itself and the abundant terraces that contribute to kilometer-baseline roughness.

The short-baseline roughness of all subunits is similar for craters and units older than Eratosthenian (systematic differences are much less than the natural roughness variability). At these ages, topographic roughness reaches equilibrium, when any additional regolith formation or creep does not cause further smoothing because it is compensated by roughening through the continuous formation of subbaseline craters (e.g., Kreslavsky et al., 2013). The equilibrium roughness on tilted walls (CW) and near-horizontal floors
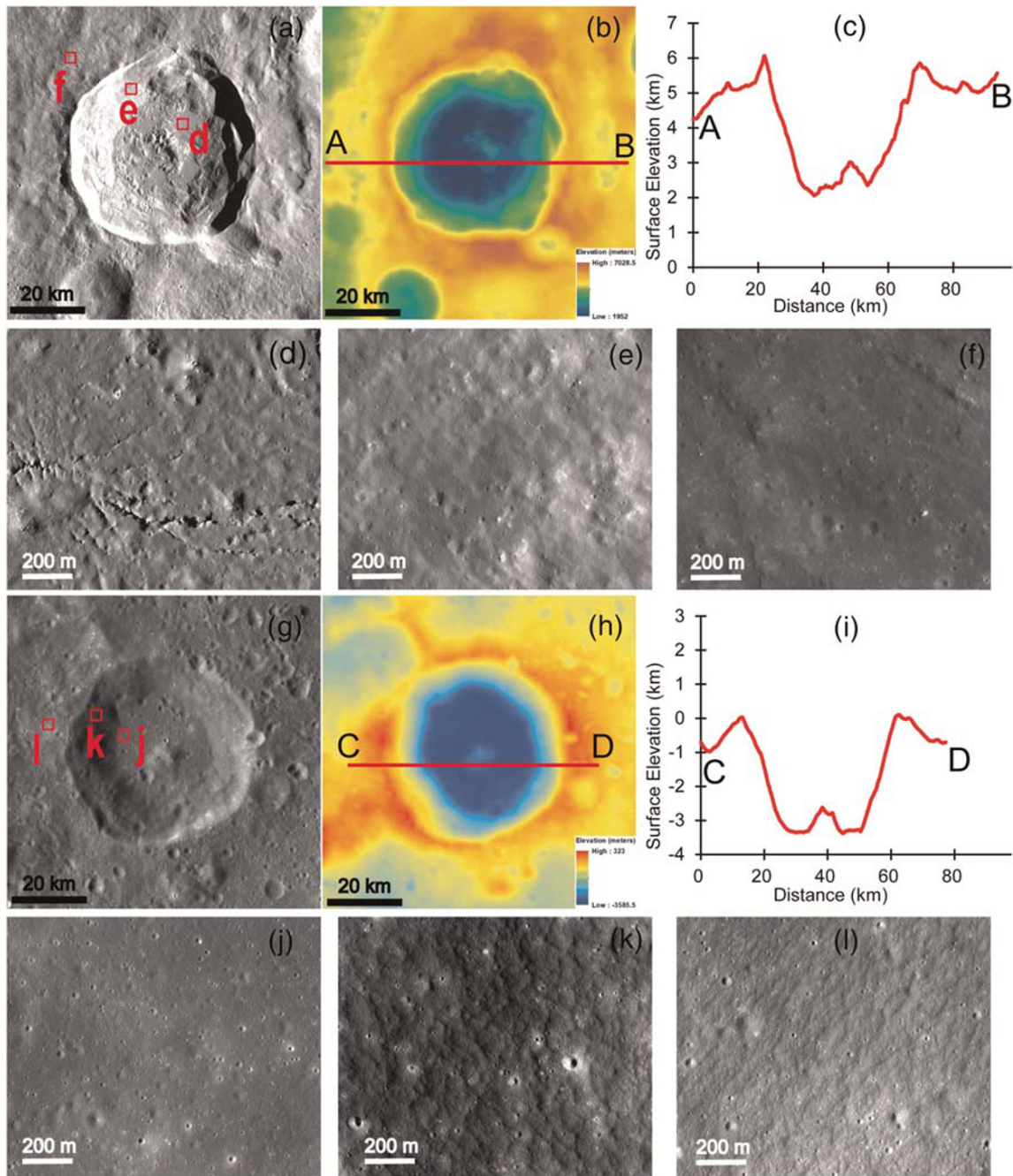
Figure 7. Subunits of fresh and degraded craters. (a) LROC WAC image mosaic of Copernican age crater Crookes. The locations of images (d)–(f) are shown by red squares and letters. (b) Topographic map of crater Crookes from LRO LOLA data. (c) A-B topographic profile across the Crookes center. (d) LROC NAC image M103231584LC showing rough floor (subunit CF) with blocks and cracks. (e and f) LROC NAC images M115034685RC and M112679355LC showing crater Crookes's wall (CW) and continuous ejecta (CE), respectively. (g) LROC WAC image mosaic of Nectarian age crater Kapteyn. The locations of images (j)–(l) are shown by red squares and letters. (h and i) The same as (b) and (c) for crater Kapteyn. (j) LROC NAC image M1214964936RC showing flat regolith-covered floor (CF) of Kapteyn. (k and l) LROC NAC images M1214964936RC and M1279660472RC showing crater Kapteyn's wall (CW) and continue ejecta (CE), respectively.

(CF) and ejecta (CE) are almost the same because the large-scale tilt of the walls is effectively filtered out by the roughness calculation procedure (Figures 7j–7l).

CE shows a significant roughness decrease with age only from the Copernican to the Eratosthenian periods (Figure 6). In stating that the decrease is significant, we mean that the difference between the median
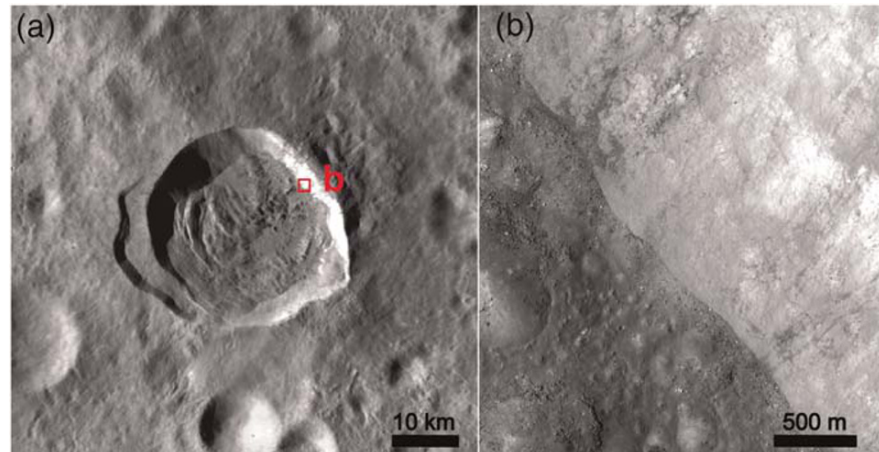
Figure 8. Blocks slid and rolled off the wall of Necho crater. (a) LROC WAC mosaic image showing Necho crater and the location of the image shown in Figure 8b. (b) LROC NAC image M1281656707LC showing the detail of boulders and blocks slid and rolled.

roughness of Copernican and Eratosthenian craters is not small in comparison to the natural scattering of roughness values for individual craters. Statistical tests indicate the formal significance of the difference at very high confidence levels; for example, for the shortest baseline, the Kolmogorov-Smirnov test rejects identical roughness-frequency distributions at significance (also known as the p value) of 3×10^{-5}. However, for all ages older than Copernican, roughness is almost the same (Figure 6); the variations of the median values are significantly smaller than the natural scattering of the roughness values between individual craters. This means that the topographic roughness of CE decreases more effectively with time early in the history of the crater, and then roughness at these scales will no longer change after it reaches a certain level; in other words, the CE reaches roughness equilibrium easily. Two factors contribute to this. First, the roughness of CE for Copernican craters is lower than that of other subunits of those same craters, which means that the pristine roughness of CE is lower, and CE is originally closer to equilibrium roughness than the other subunits. Second, at larger scales, CE is essentially flat (Figure 7), and regolith transport from local highs to local lows effectively removes topographic variations. CF and especially CW, however, have significant topographic amplitudes (Figure 7) that reduce the effectiveness of degradation processes.

Fassett and Thomson (2014) described the degradation of small craters as diffusion creep and obtained a diffusivity of ~5.5 m²/Ma from their observations. This value gives ~2 Ga for the characteristic time scale of degradation of hundred meter features in the horizontal dimension. This is consistent with equilibrium roughness having been reached for Imbrian craters but not for Copernican or Eratosthenian craters.

In contrast to the short baselines, the long-baseline roughness of the older crater walls (CW) is higher (Figures 5, 7e, and 7k) because the crater topography itself affects the long-baseline roughness at all ages. At these length scales, the roughness never reaches equilibrium values, and the rough signature of the crater walls and their terraces persists for all ages through the Nectarian. However, there is a prominent age trend: older craters have progressively smoother walls.

Except for the Copernican craters, there is a weak increasing trend of CE roughness with age for long baselines; this seemingly contradicts our interpretation of ongoing degradation and attainment of equilibrium. We attribute this to an observational bias: for craters, the CE subunit can be mapped only near rim crests of older craters because the topography of the discontinuous ejecta materials has been entirely degraded and become indistinguishable from the background. Therefore, long-wavelength elevated rim topography affects the roughness signature more effectively for older craters.

3.2. Rock Abundance and Soil Temperature

Our results (Figure 5) confirm increased rock abundance and soil temperature for young craters (Bandfield et al., 2011; Ghent et al., 2016). This correlation is easy to explain: The immature regolith of younger craters
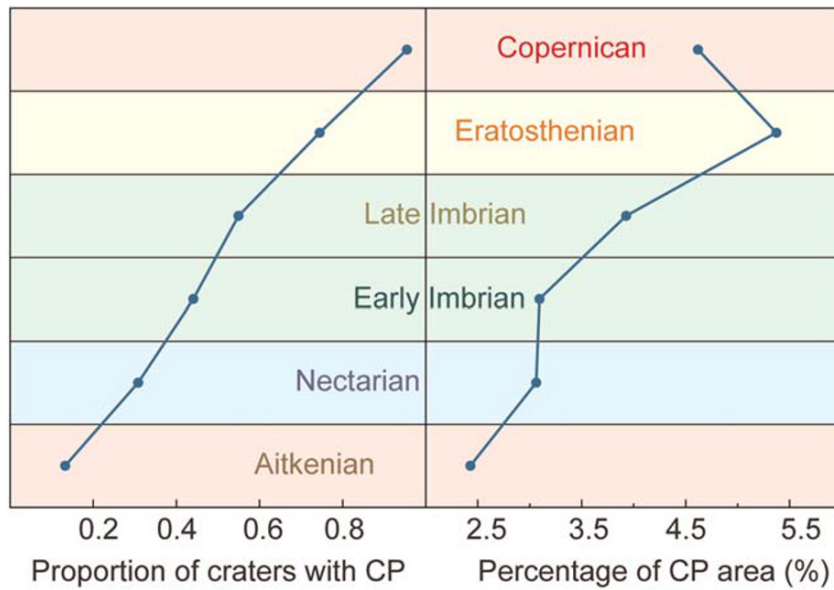
Figure 9. The proportion of craters with mapped central peaks in left side, and the average percentage of crater area occupied by the central peak unit among craters with central peaks, as a function of stratigraphic age, which is plotted along the vertical axis. Only craters larger than 40 km are used.

contains an increased proportion of rock fragments (these, when exposed at the surface, control the rock abundance parameter) and pebble- and sand-sized particles (these, together with shallowly buried rocks, affect the nighttime soil temperature). With time, rocks and large regolith particles disintegrate due to a number of factors including subsequent impacts and thermal stresses (Basilevsky et al., 2013).

For CE, the age trend of rock abundance is observed only for the Copernican craters (Figure 5), in a manner similar to that of the short-baseline roughness, partly for the same reason: For CF and CW, slopes are preserved for a longer time due to their greater topographic amplitudes, and intensive downslope migration of regolith exposes bedrock. This does not happen for CE: As soon as the roughness reaches equilibrium, steep slopes disappear, and regolith reaches the equilibrium maturity level soon after that. Another important cause of roughness and rock abundance decrease in CE is depositional processes, especially in more rugged terrain. The rapid decrease of rock abundance of CE is consistent with the observation that circular polarization ratio enhancements in the crater exterior fade faster than in the crater interior (Fa & Eke, 2018; Fassett et al., 2018).

The thermophysical properties of both CW and CF subunits are almost the same, with the exception that the rock abundance for the Copernican craters (Figure 5) is noticeably higher for CF than for CW while their nighttime soil temperatures are similar. We suggest that there may be two factors that are responsible for this. First, large blocks slide or roll down from the steep sections of the walls and are preserved at the floors or piled at the base of steep sections, thus reducing the smooth area of the crater floor. This corresponds to the hundred meter baseline roughness measurement of the Copernican craters. Evidence for blocks sliding and rolling off the walls is visible in high-resolution images as well (Figure 8). Second, significant proportions of the floors are covered by impact melt. In general, impact melt rocks should be more competent than the fractured and brecciated materials dominating the walls and ejecta, and such materials could be more easily disintegrated into fine grains. In high-resolution images (Figures 7 and 8) it is readily seen that the Copernican crater floors retain their sharp pristine morphology with many resolved rocks and large blocks (Dhingra et al., 2017); thus, the measured distinction in the rock abundance appears to be supported by morphological observations.

3.3. Central Peaks

Central peaks (subunit CP, Figure 1) are very diverse in their characteristics, and the areas they cover are generally small in comparison to the areas of the other subunits, often being too small for roughness
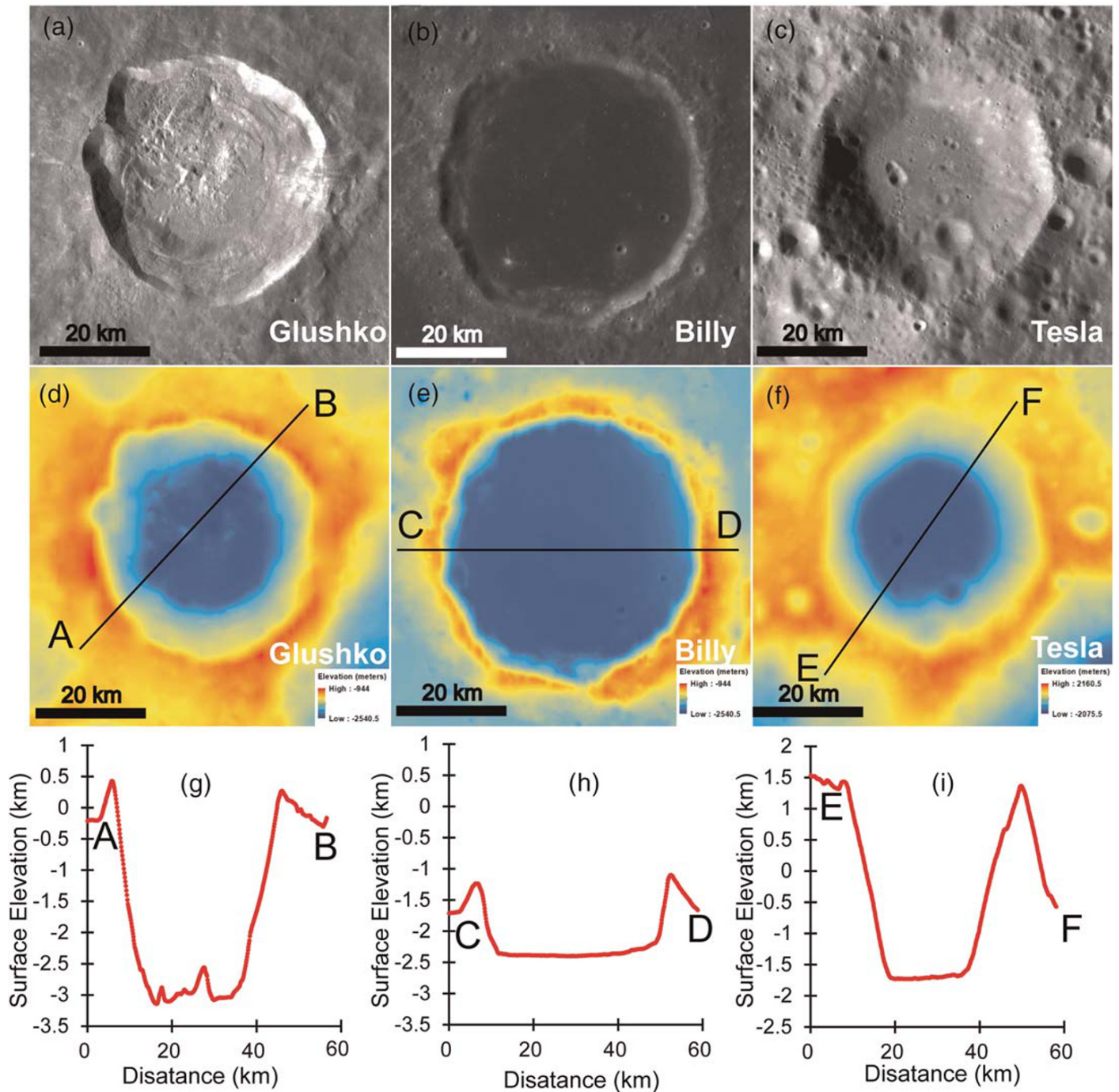
Figure 10. Comparisons of fresh and infilled craters. Panels (a), (d), and (g) are image, topographic map, and topographic profile, respectively, of crater Glushko. Glushko is a Copernican age crater whose central peak is retained completely. Panels (b), (e), and (h) are the same for the crater Billy. Billy is a Nectarian age crater whose floor was infilled by thick volcanic deposit causing shallow depth. Panels (c), (f), and (i) are the same for crater Tesla. Tesla is also a Nectarian age crater; however, it was filled with light plains material (Meyer et al., 2020). Its central peak is presumably degraded and buried; however, the crater retains a significant depth. Panels (a)–(c) are LROC WAC image mosaic. Panels (d)–(f) are digital elevation models from LOLA data.

calculations. This is the reason we did not consider CP in the previous sections. However, the presence of the central peaks (or peak rings) (Figure 9) shows a very pronounced trend. Almost all large ($D > 40$ km) Copernican age craters in the crater database have central peaks (Baldwin, 1972, 1981; Grieve, 1987; Melosh, 1989; Melosh & Ivanov, 1999). A single Copernican crater without a CP subunit actually has a
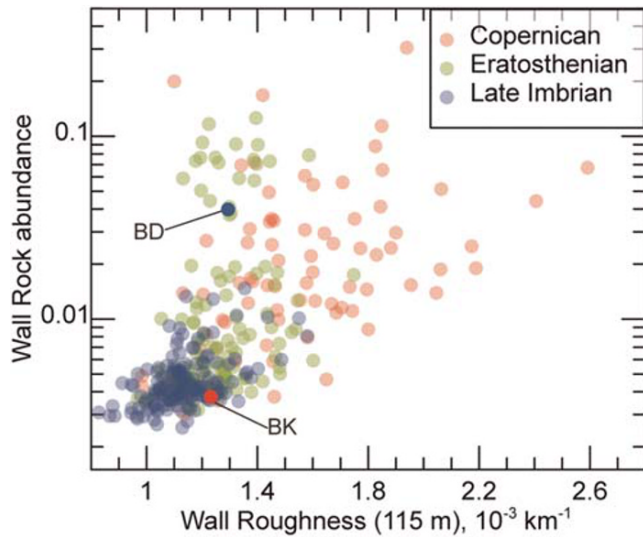
Figure 11. Scatter plot of rock abundance and wall roughness at 115 m baseline. Colored dots show individual crater walls of different stratigraphic ages. BD, Bonpland D; BK, Bel'kovich K.

central peak, but it is too small to be mapped in the frame of the 1:2,500,000 global mapping project. The proportion of craters with central peaks systematically declines with age (Hale & Head, 1979; Head, 1975). In contrast to the roughness and thermophysical properties, this decline is not limited to the younger craters, continuing through the older ones. The oldest, Aitkenian craters are almost devoid of central peaks. The area occupied by central peaks in craters where they are present also systematically decreases with stratigraphic age (Figure 9).

The observed trends clearly indicate that infill of craters makes an essential contribution to crater degradation (Head, 1975). Central peaks and peak complexes in large craters are several kilometers across; local diffusive regolith transport cannot completely eliminate such features because it does not eliminate craters of comparable size. We clearly see morphological and spectral evidence of the infill of some large craters with volcanic material (e.g., Whitten & Head, 2013). Some craters are filled with light plains material (Meyer et al., 2020), which is spectrally identical to highlands material but shows an apparent embayment morphology (Figure 10). The embayment morphology in the oldest craters is not apparent (Figure 10) but the observed trend of central peak occurrence indicates that these craters were also filled with light plains material.

3.4. Age Determination

As we described above, younger craters have distinctive roughness and thermophysical properties that evolve with age and approach global average, equilibrium values (Figures 5 and 6). This points to an interesting opportunity to determine crater ages on the basis of those trends. High values of topographic roughness, rock abundance, and soil temperature would suggest that a crater is generally young. Extremely high values would suggest a Copernican age. Regular rock abundance value and moderately high short-baseline roughness would suggest an Eratosthenian age.

However, there are some important limitations to such an approach. First, roughness (except crater walls at the longest baseline) and thermophysical attributes for Imbrian and all earlier craters are already similar to the equilibrium values and are indistinguishable from the background. Therefore, this age-assessment method is in principle applicable only for Copernican and Eratosthenian ages. Second, despite the conspicuous age trends, individual variations in the attributes are comparable in magnitude to the systematic differences. Figure 11 shows a scatterplot of wall roughness and rock abundance, clearly illustrating that the domains of parameter values for different stratigraphic ages overlap significantly. The same occurs for other pairs of parameters (supporting information Figure S3). We interpret this to be due in part to the inherent noise in roughness and thermophysical properties, in part due to the natural variability of lunar craters, and partly due to the possibility of nonuniform degradation, such as a rapid change of parameters due to proximity weathering (Head, 1975). This means that roughness and thermophysical parameters are not simple functions of age and are affected by many other factors; therefore, they alone cannot be used reliably for the independent age determination of individual craters.
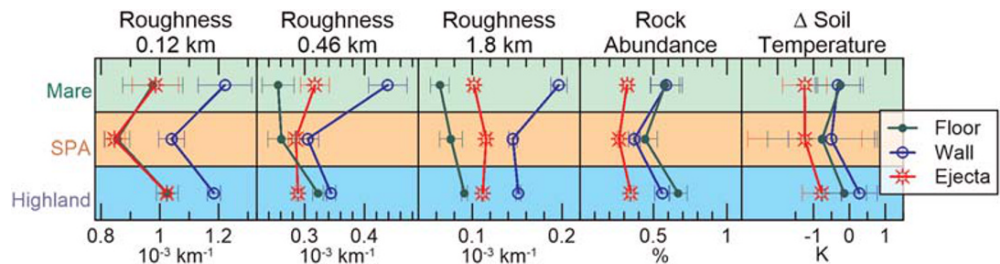

Figure 12. Median topographic roughness (115, 460, and 1.8 km baselines), mean rock abundance, and median soil temperature for craters in the three terrain types. Only craters larger than 40 km of Copernican, Eratosthenian, and Late Imbrian ages were used to calculate the median and mean values. Error bars represent standard errors.
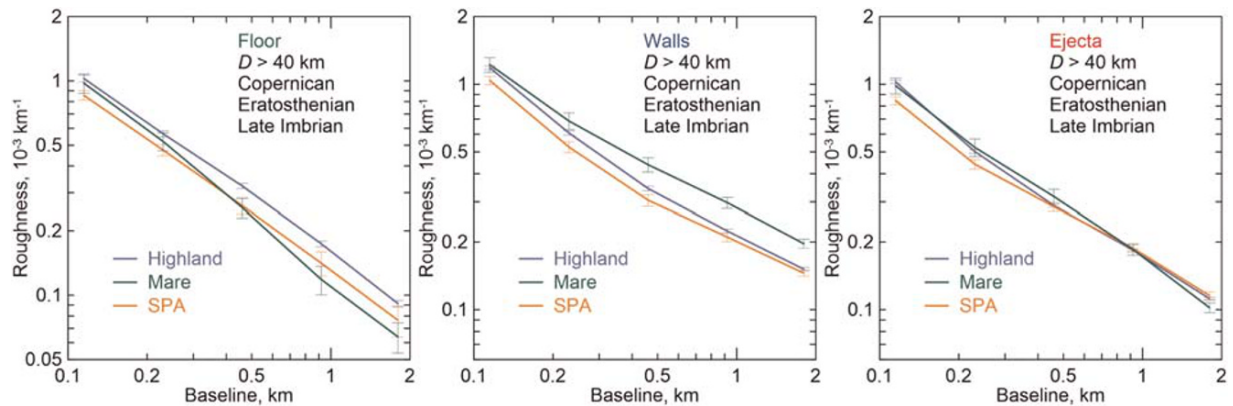
Figure 13. Topographic roughness trends with baselines for younger craters in three terrains for the crater floor subunit (left), crater wall subunit (middle), and continuous ejecta subunit (right). All plotted quantities are calculated for craters of younger stratigraphic ages only: Copernican, Eratosthenian, and Late Imbrian. Error bars represent standard errors.

Recently, Mazrouei et al. (2019) applied a measure derived from the Diviner rock abundance data as a proxy for age for craters less than ~1 Ga. Such an approach may be valid when the inferences are derived from statistics of many craters, as has actually been done in their work. Our results, however, indicate that the values obtained from the regression suggested by Ghent et al. (2014) and Mazrouei et al. (2019) should not be considered as robust age estimates for individual craters. On the other hand, the various parameters can be used as powerful supporting information; in particular, they give us clues to the detection of potentially misclassified stratigraphic ages, which we discuss in section 6.

4. Systematic Differences Between Terrains

In this section, we analyze the effects of the target material on the quantitative characteristics of crater subunits based on the three different terrain types (section 2.2). Since the maria underwent an extensive volcanic resurfacing in the Imbrian period (Hiesinger et al., 2011; Wilhelms et al., 1987), they do not have large, older craters. To exclude the age bias, in this section we analyze craters of younger stratigraphic ages only: Copernican, Eratosthenian, and Late Imbrian. Although within each terrain the measured characteristics vary over a wide range due to the difference in the degree of crater degradation (section 3) and individual differences between craters, consistent trends are seen in Figures 12 and 13.

4.1. Topographic Roughness

At the shortest baseline, there is no systematic difference between craters in the maria and the highlands (the difference in median roughness is much less than the natural roughness variability). The median roughness calculated over all craters is dominated by the Late Imbrian craters, whose shortest-baseline roughness is already close to the equilibrium value. The short-baseline roughness is generally similar for craters in the maria and highlands (Kreslavsky et al., 2013).

At short baselines, the South Pole-Aitken (SPA) craters appear smoother than craters on the other terrains, a trend that occurs for all crater material subunits (Figures 12 and 13). We found that an observational bias may be partly responsible for this: The craters of different stratigraphic ages in the database were unevenly distributed among the three terrains. In particular, the proportion of stratigraphically younger craters was lower in the SPA terrain than in the other two. The fewer number of young craters in SPA terrain might be due to the relatively lower impact rate at high latitudes (Le Feuvre & Wieczorek, 2011) combined with a higher proportion of high latitudes in the SPA. Crater roughness decreases with age, so the relative shortage of young craters in the SPA terrain would cause lower median roughness.

We excluded the potential observational bias by considering only the Late Imbrian craters (supporting information Figure S4); however, we still see that SPA craters are smoother. This effect is rather strong, and we do not see any further observational biases that could explain it. The typical background roughness (outside of the young crater materials) in the SPA region is also lower than in typical highlands (Kreslavsky et al., 2013),
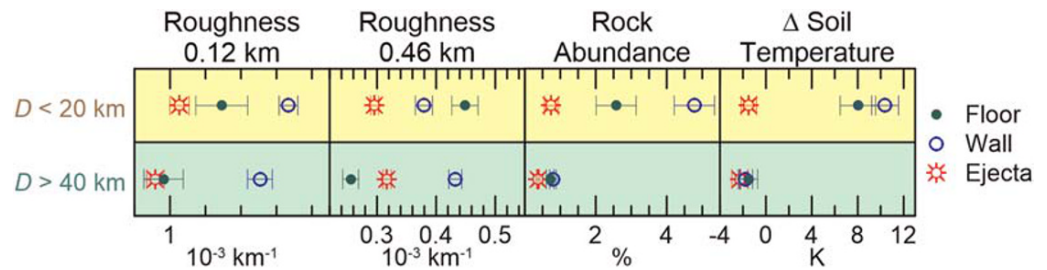
Figure 14. Roughness, rock abundance, and soil temperature for Copernican and Eratosthenian craters of different sizes in the maria (craters with $D < 20$ km on top, $D > 40$ km on bottom). Error bars represent standard errors.

which is likely to be a related phenomenon. The absence of such an effect (for CW, CE, and the background) at long baselines suggests that SPA smoothing is caused by surficial processes; therefore, it is unrelated to the crustal thickness. The compositional differences between SPA and other highlands are related to the presence of distinctive mineralogies within the basin interior (Moriarty Iii & Pieters, 2018), most likely linked to the presence of an extensive ancient impact melt sheet on the SPA floor (e.g., Vaughan & Head, 2014), mixed impact melt and deep crustal materials in the surrounding areas, and the possibility of ancient cryptomeria (e.g., Whitten & Head, 2013) obscured by more recent craters and ejecta from the Orientale basin. In the broadest sense, the SPA composition and mineralogy should be between typical highlands and maria, and if composition and mineralogy were responsible for the roughness differences, we would expect the SPA roughness also to be between highlands and maria, which is not the case. However, we cannot rule out the presence of unusual lithologies in the interior of the SPA, the largest and most ancient basin, that could have an effect on rock breakdown and roughness processes and rates.

It is possible that the latitudinal trend in the impact rate is partly responsible for this effect. The short-baseline roughness reflects a balance between roughening by the baseline-scale craters and smoothing by regolith gardening. A lower impact rate at high latitudes (Le Feuvre & Wieczorek, 2011) would mean fewer young, small (baseline-scale) craters, and therefore a smoother equilibrium topography than if the regolith gardening processes have a weaker latitudinal dependence. However, the global roughness spatial pattern (which, we believe is related to the trend in crater roughness) differs significantly from the pattern related to the cratering rate (Kreslavsky et al., 2013). Therefore, the spatial variations of the impact rate are unlikely to be the only cause of the observed smoothness of SPA.

At longer baselines, walls of craters on the maria are systematically rougher than crater walls in highlands and the SPA (Figures 12 and 13). Generally, the high roughness of the walls of large craters is caused by numerous terraces, whose spatial scale is comparable to the baseline (Figure 4). The observed difference can be explained by a higher mechanical strength of competent volcanic material of the maria in comparison to a weaker, heavily fractured highlands megaregolith (e.g., Cintala et al., 1977). It is possible that the wall terraces in mechanically stronger, naturally layered mare material is originally rougher than in the highlands. It is also possible that higher resistance to degradation of mechanically stronger mare material plays a role: Since roughness decreases with crater age, higher resistance to degradation would allow the roughness to persist longer. This effect is partly similar to a higher abundance of very steep slopes in mare craters noted by Kreslavsky and Head (2016).

At the longest baseline, crater floors are significantly smoother than walls, ejecta, and typical roughness of the highlands. Some Late Imbrian age craters have floors filled with lavas, which make floors exceptionally smooth at longer baselines. A more significant factor is the presence of impact melt in these large craters that makes the floors horizontal and flat at the baselines longer than the characteristic scale of blocks on the floor. Floors of craters on the maria, in general, are slightly smoother than on the highlands. Two factors can explain this. First, the proportion of craters filled with lavas, and hence possessing exceptionally smooth floors, is higher on the maria due to the more extensive Imbrian period volcanism there (e.g., Head & Wilson, 1992; Hiesinger et al., 2011; Wilhelms et al., 1987). Second, the difference in the mechanical properties can affect energy partitioning in the impact process, which might be responsible for a generally higher proportion of melted material, and a higher amount of impact melt, which makes floors flatter (Cintala et al., 1977; Cintala & Grieve, 1998; Melosh, 1989). Additional detailed morphological observations of groups of individual craters are needed to distinguish which of the two factors dominates.

Table 1
Craters Listed as Copernican That Appear to be Misclassified

Crater name	Latitude	Longitude	Diameter (km)
Autolycus	30.68°N	1.49°E	38.88
Bel'kovich K	63.63°N	93.61°E	47.03
Birkhoff Z	60.98°N	145.88°W	28.63
Carpenter	69.52°N	51.23°W	59.06
Eudoxus	44.27°N	16.23°E	70.16
Mosting	0.70°S	5.88°W	24.38
O'Day	30.42°S	157.29°E	70.41
Taruntius	5.50°N	46.54°E	57.32
Virtanen	15.64°N	176.74°E	39.65

4.2. Rock Abundance and Soil Temperature

Systematic differences in the thermophysical properties between craters on the different terrains (Figure 12) are minor (note that the rock abundance and soil temperature axes in Figure 12 are stretched in comparison to Figure 5). This is naturally explained by the fact that the high rock abundance and soil temperature of pristine craters disappear relatively quickly: Craters older than Copernican have thermophysical properties close to the equilibrium value, and such craters dominate the analyzed subset. This is also consistent with a short (~100 Ma) timescale of the disintegration of large boulders, which has been derived from independent observations (Basilevsky et al., 2013).

This absence of a difference between maria and highlands in thermophysical properties seems at odds with the slightly higher soil-temperature values and noticeably higher rock abundance on the maria seen in the global thermophysical-properties maps. Elevated rock abundance in the maria is caused by rocks produced by small impacts (Bandfield et al., 2011; Haber et al., 2018). A greater number of resolved rocks associated with small impacts in the maria is apparent in the high-resolution images. Our data for crater subunits for the smaller craters in the database ($D < 20$ km) shows significantly higher rock abundance and soil temperature on mare surfaces (supporting information Figure S5) for crater walls and floors, in contrast to those observed for larger ($D > 40$ km) craters (Figure 12). The proportion of younger craters among the smaller-crater ($D < 20$ km) subset in the catalog is higher; therefore, the younger craters affect the characteristic values of thermophysical properties for this size range. Thus, relatively small ($D < 20$ km) craters produce many more rocks on mare surfaces in comparison to the highlands. An analogous trend is observed for the soil temperatures of floors and walls of smaller ($D < 20$ km) craters.

We interpret this to be due to two factors: (1) Contributions by the competent volcanic substrate material of the maria, which, upon being impacted, produces more rocks and coarse soil particles than heavily fractured megaregolith of the highlands (Bandfield et al., 2011; Mustard & Head, 1996; Shkuratov et al., 2011), and (2) the thinner regolith of the maria means that solid bedrock is more readily encountered by craters in the maria than those in the highlands. This is supported by observations with high-resolution LROC images, which show that small impacts into melt sheets expose rocks that are clearly visible (Bandfield et al., 2011).

Craters in SPA show a slightly lower rock abundance and soil temperature than in the maria and typical highlands; this occurs for all crater material subunits. We suggest that an unusual substrate in the SPA basin interior or the paucity of younger craters in SPA in the crater database could account for the lower observed rock abundances and soil temperatures.

5. Differences Between Simple and Complex Craters

In the previous sections, we have discussed large complex craters with diameters larger than 40 km. As we noted above, craters can be generally divided into simple and complex (Figure 4). On the Moon, the simple-to-complex transition occurs between 15 and 20 km in diameter (Pike, 1977b). Here (Figures 14 and S6) we select 20 km as the upper-diameter limit for the subset of small craters; therefore, this subset spans the range from simple to complex. Further lowering this diameter limit would compromise the statistical validity of the analysis.

Two introductory points should be noted. First, the age-sized distribution of the simple craters in the database is strongly biased, in that almost all belong to the Copernican and Eratosthenian periods, though older simple craters undoubtedly exist on the Moon. This bias occurred because only the more prominent craters were named and included in the database. To avoid the effects of this bias in this section, we consider only Copernican and Eratosthenian craters. Second, the smaller craters in the database are preferentially located in the maria. To avoid this bias, we focused on the maria only in this study.

We note that the longer roughness baselines are not suitable for the smaller craters, because roughness cannot be calculated for a baseline, which is on the same order of magnitude as the size of the subunit.
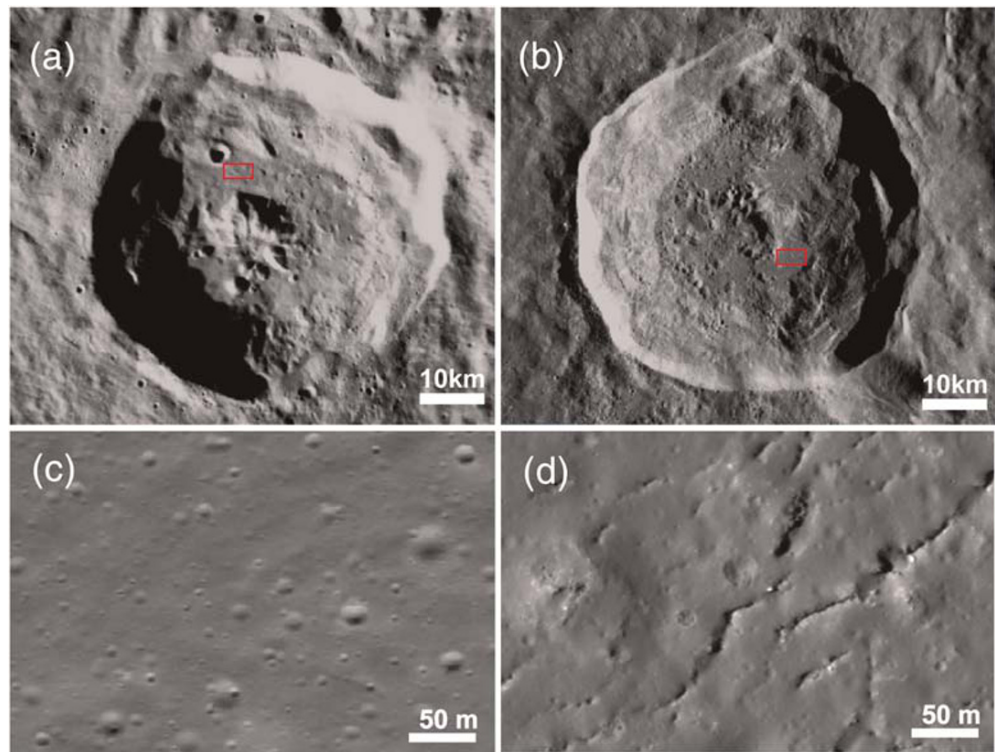
Figure 15. Comparison between Bel'kovich K (misclassified as Copernican age) and Crookes (typical Copernican age) craters. (a and b) The upper images are LROC WAC images in orthostatic projection. (c and d)The bottom images are NAC high-resolution images. Younger features: solidified impact melt texture and superimposed decameter-sized craters. Older features: many decameter-sized craters with flat and smoothed features.

For example, the floor diameter of crater Kepler C, which is 11.5 km in diameter, is around 4 km. The long baseline is 1.8 km, which is on the same order of magnitude as the size of the floor subunit.

There is no significant systematic difference in the shortest-baseline roughness between small and large craters (Figure 14), which has been interpreted before. This is not the case for the intermediate-baseline roughness: Large crater floors on average are significantly smoother, and the walls are rougher than in small craters (Figure 14). The smoothness of floors of large craters is likely to be caused by their general flatness due to the presence of impact melt. The amount of impact melt in relation to crater volume or area is known to be greater for larger craters; for craters smaller than 20 km impact melt occupies a small proportion of the floor or is absent (Cintala & Grieve, 1998). On the other hand, mounds, blocks, and cracks responsible for the high, short-baseline roughness of the floors of the youngest craters (Figure 5) are much smaller than the 0.5 km baseline, and their effect at this baseline is minor. Greater wall roughness in larger craters is caused by the presence of terraces: They are typical for complex craters and are absent in simple craters, by definition. Their characteristic spatial scale is on the order of a kilometer (Figure 4), so they affect the intermediate, but not the shortest, baseline roughness.

The rock abundances and nighttime soil temperatures of small, simple craters are generally higher than for larger craters for all material subunits (Figure 14). This can be caused, at least in part, by a bias in the crater sample: the proportion of Copernican age craters in the maria is greater among small craters, and, as we discussed above, such craters are characterized by the highest rock abundances and soil temperatures. Another factor is that the walls in simple craters are steeper than in complex craters on average; therefore, intensive, downslope material transport exposing blocks and immature regolith is more active in small craters. This is consistent with walls having the highest rock abundance among the subunits. We also suggest that the difference in the scale of the impact event may be a factor. The large-scale impact events that produce complex craters are characterized by a higher proportion of melted and vaporized material, as well as higher characteristic shock pressure experienced by ejected material, which would favor more thorough disintegration of
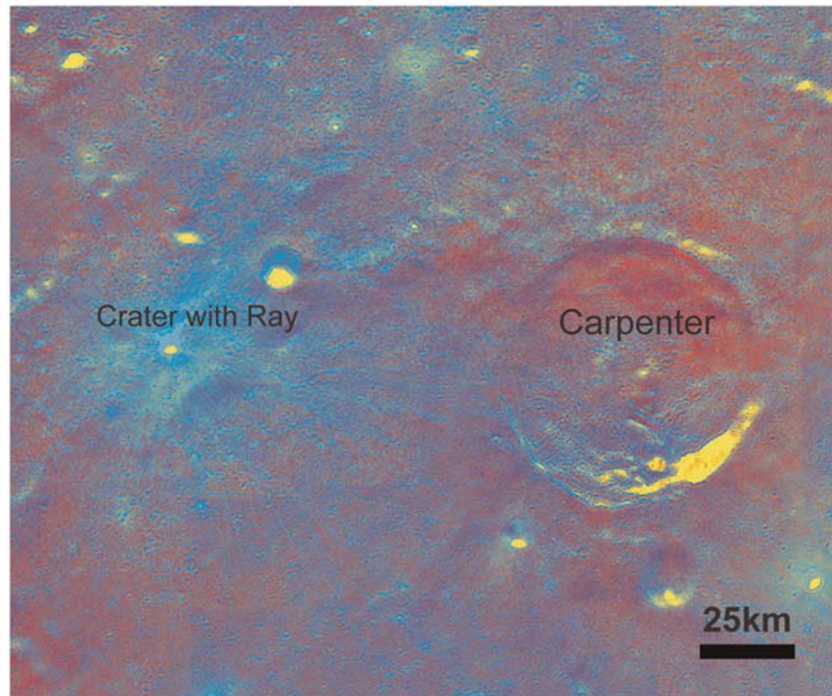
Figure 16. Ray from an unnamed crater across Carpenter crater. The image is the Clementine UVVIS ratio color image using the red channel in 750/415 nm, green channel in 750/950 nm, and blue channel in 414/750 nm.

the target material and reduce the abundance of rocks and the coarse soil fraction in the shocked material (Cintala & Grieve, 1998; Melosh, 1983; O'Keefe & Ahrens, 1999).

6. Implication

6.1. Reclassification of Crater Stratigraphic Age

Our analysis showed that the parameters for the crater walls have the highest sensitivity to age. We mainly use the scatter plots of rock abundance in the crater wall material and topographic roughness at 115 m baseline (Figure 11) to identify craters that we suspect might have a misclassified stratigraphic age. Copernican crater walls should be rougher and have more rocks.

We selected all "suspicious" craters that are classified as Copernican but have low values of short-baseline topographic roughness, rock abundance, and soil temperature, which is the domain where all Imbrian and older craters normally reside. Then we checked high-resolution images of all those craters. We found that the morphologies of nine craters are inconsistent with a Copernican age (Table 1). All of them appear older, perhaps Eratosthenian or, in some cases, even Imbrian. These craters have morphological signatures of thick regolith: Typical impact melt textures on the crater floors are not distinguishable; there are few boulders or signs of geologically recent landslides; superposed craters do not possess morphologies that are suggestive of a thin regolith layer; and there are many superposed, shallow, smoothed, decameter-sized craters. As an example, in Figure 15 we compare crater Bel'kovich K with the typical Copernican crater Crookes, which is similar in size.

The misclassified craters had been originally assigned to the Copernican period on the basis of bright rays associated with them (Hawke et al., 2008; Wilhelms et al., 1987; Wilhelms & Byrne, 2009). Hawke et al. (2004) analyzed spectral signatures of several rays and showed that the rays can be caused either by low regolith maturity ("maturity rays"), an admixture of excavated highland material on mare surfaces ("compositional rays"), or a combination of the two. They argued that the attribution of craters having purely compositional rays to the Copernican could be erroneous. In particular, Hawke et al. (2004) argued that Autolycus has purely compositional rays and therefore is older than Copernican. We included
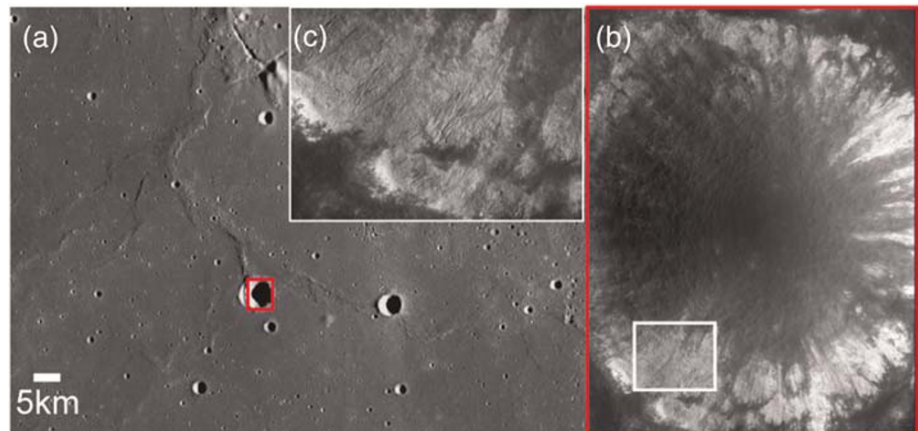
Figure 17. Crater Bonpland D. (a) Regional context of Bonpland D; the red frame outlines the view shown in (b). WAC mosaic image with large shadows (643 nm wavelength). (b) Crater Bonpland D with bright regolith flows on the walls. The white rectangle indicates the area shown in (c). (c) A detail of the dry regolith flows. Panels (b) and (c) are from LROC NAC image M1190835853RC.

Autolycus in Table 1 (inconsistent with a Copernican age) on the basis of its roughness signature and small-scale morphology; thus, it appears that Hawke et al. were correct in their assessment. Another possible cause of misclassification is that a crater is occasionally located at crossing rays originating from different craters. Kreslavsky et al. (2013) noted that the crater Taruntius was misclassified and suggested a ray-crossing explanation for its original misclassification (Wilhelms & Byrne, 2009). A clear example of this kind is crater Carpenter in Figure 16, which is crossed by a ray from a very young unnamed 5 km crater at 69.7°N 61.0°W and is older than Copernicus (McEwen et al., 1993).

6.2. Recent Active Geological Processes

An unusual combination of properties for some craters does not necessarily mean misclassification but could reflect interesting individual peculiarities of a crater. For example, the Late Imbrian crater Bonpland D (BD in Figure 11) has an unusually high rock abundance on its walls (subunit CW), well outside the range for Late Imbrian craters, while its roughness signature is consistent with this age. The soil temperature of its wall material is also anomalously high.

Bonpland D (10.2°S, 18.3°W, $D = 5.3$ km) is situated in Mare Cognitum and embayed by mare-forming lavas (Figure 17). According to Hiesinger et al. (2003), the absolute crater-retention model ages of the mare units embaying Bonpland D are 3.41 and 3.49 Ga, which is within the Late Imbrian Period. McCauley and Wilhelms (1971) also mapped this mare as Imbrian in age. There are no signs that Bonpland D was affected by Imbrium ejecta, which suggests that it postdates the Imbrium impact. On the other hand, the lavas with cratering-derived model age of 3.49 Ga (Hiesinger et al., 2011) do not breach the rim, nor do they fill the crater interior, which suggests that the Bonpland D postdates the early stages of Mare Cognitum volcanism. Therefore, the Late Imbrian age of Bonpland D is very certain. The crater is crossed by a wrinkle ridge (Figure 17), which seems to deflect from its regional NW-SE trend toward the SW to the crater; therefore, the formation of the ridge appears to postdate the impact. A part of the western crater wall is displaced (Figure 17). This displacement is morphologically different from wall terraces observed in impact craters, and the presence of wall terraces is unlikely for simple craters of this size. Therefore, the displacement was likely caused by a fault associated with the wrinkle ridge.

In high-resolution images of this crater (Figure 17), we observe that a general rim softness and an apparently thick regolith are indeed consistent with the Late Imbrian age; the displacement of the western wall is also geologically old because a thick regolith layer is seen there, too. The conclusions about the thick regolith are based on the small-scale morphological signatures, which can be seen in Figure 18. These signatures include the absence of boulders, the absence of superposed decameter-size double-ring craters that typically occur in a thin regolith layer, and abundant superposed shallow subdued decameter-sized craters. However, the inner crater walls contain numerous small channels and associated lobate flows apparently formed by
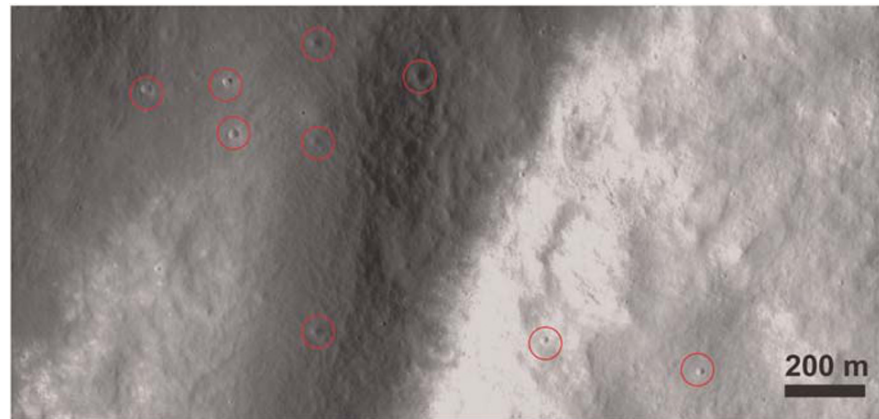
Figure 18. Morphological indications of thick regolith for Bonpland D. The image is from LROC NAC image M1190835853RC. Red circles show younger and older decameter-sized craters.

regolith flows. These flows have some similarities to regolith flows described by Shkuratov et al. (2012), Senthil Kumar et al. (2013), and Kokelaar et al. (2017) in large Copernican craters. They are not morphologically identical to those flows, however, because in Bonpland D, unlike the Copernican case, the flows are formed from older, thick regolith. These regolith flows apparently expose formerly buried rocks (the largest of these are indeed seen in the images), which results in the observed high rock abundance and soil temperature. The thermophysical signatures and high albedoes of the immature regolith of the flows indicate their Copernican age. The exceptional sharpness of tiny flow lobes on these slopes is consistent only with their very young geological age, tens of Ma, or even younger.

Bonpland D is the oddest crater in our data set, which is old, not Copernican and Eratosthenian, and presents an unusually higher rock abundance on its wall. We interpret the unusual case of regolith flows in Bonpland D to be caused by geologically recent local strong seismic events, which fluidized the regolith by shaking and triggered numerous slides on an otherwise stable slope. Such an event is likely to be caused by reactivation of the shallow wrinkle-ridge-associated fault. Triggering by a local or nearby impact is excluded because there are no suitable small fresh craters inside Bonpland D, or larger craters in its vicinity, that would have initiated small-scale features as sharp as the regolith flow lobes in Bonpland D. Triggering by large distal impact events or by deep high-amplitude moonquakes is excluded because it would cause widespread slides and therefore would not account for the uniqueness of Bonpland D.

Our inference about recent strong seismicity is not unique. For example, Senthil Kumar et al. (2016) analyzed traces of rolling boulders on slopes and suggested geologically recent seismic events in association with lobate scarps in the Schrödinger basin. Lobate scarps (e.g., Watters et al., 2015, and references therein) are thought to be geologically young tectonic features and sources of shallow seismicity. No lobate scarps have been mapped (Watters et al., 2015) in the immediate proximity of Bonpland D; however, there are possible geologically recent lobate scarps in association with wrinkle ridges at the northeast edge of Mare Cognitum (Nelson et al., 2014). Shallow seismic events detected by Apollo seismometers (Nakamura et al., 1982) are too weak to mobilize regolith; however, they unambiguously indicate the presence of shallow seismicity on the Moon. Locations of shallow seismic events detected by Apollo (Watters et al., 2019) do not coincide exactly with Bonpland D, but there is an inferred epicenter location in Mare Cognitum.

7. Conclusions

We studied the characteristics of lunar crater materials quantitatively by dividing them into subunits rather than treating them as a single unit. We analyzed the variations of subunit characteristics as functions of age, location, and crater size.

Younger craters always have higher values of topographic roughness, rock abundance, and nighttime soil temperature. The crater subunits degrade with age due to smaller impacts, mass wasting, regolith transport, and other surface processes. Among the subunits, the continuous ejecta reaches roughness and rock

abundance equilibrium more rapidly than the other crater subunits. We suggest that this occurs because the original ejecta roughness is relatively low and therefore closer to the equilibrium value, and also because the continuous ejecta is flat at large scales, increasing the efficiency of terrain smoothing by regolith transport.

We found some regional variations of roughness and thermophysical parameters for crater by subdividing the lunar surface into three terrains: maria, highlands, and the South Pole-Aitken basin. Craters located on the maria have systematically rougher walls at longer baselines, with more rocks formed during the impact event, which we attribute to the mechanically stronger volcanic material of the maria. Craters located in the SPA terrain have systematically lower short-baseline topographic roughness, rock abundance, and nighttime soil temperature. This remains unexplained and needs more analysis. The dependence of the impact rate on latitude might contribute to this.

Crater size can also affect the observable signatures. The smaller, simple, and transitional craters show higher rock abundance than larger complex craters.

Due to their strong dependence on age, the quantitative parameters that we analyzed (topographic roughness, rock abundance, and nighttime soil temperature) are very useful for validation of ages derived from stratigraphic and morphological considerations, especially for Copernican and Eratosthenian craters. We caution, however, that these parameters alone cannot be reliably used for age determination due to the wide natural variability of their values.

Analyses of those parameters revealed several craters with unusual characteristics. We analyzed the most outstanding of these: The Late Imbrian-aged crater Bonpland D in Mare Cognitum. We found that its walls have numerous, geologically very recent, small regolith flows, which result in an unusually higher rock abundance and that are not observed in other craters of Late Imbrian age. We interpret them to be caused by geologically recent strong shallow seismic events.

Data Availability Statement

All of the data used in this work are accessible in the NASA Planetary Data System. All the data necessary to generate the results used for this study are available online (https://doi.org/10.6084/m9.figshare.10298039.v1).

References

Agarwal, N., Haridas, A., Khanna, N., Srivastava, P., & Jain, V. (2019). Study of morphology and degradation of lunar craters using Chandrayaan-1 data. *Planetary and Space Science*, *167*, 42–53. https://doi.org/10.1016/j.pss.2019.01.003

Baker, D. M. H., Head, J. W., Phillips, R. J., Neumann, G. A., Bierson, C. J., Smith, D. E., & Zuber, M. T. (2017). GRAIL gravity observations of the transition from complex crater to peak-ring basin on the Moon: Implications for crustal structure and impact basin formation. *Icarus*, *292*, 54–73. https://doi.org/10.1016/j.icarus.2017.03.024

Baldwin, R. B. (1972). The tsunami model of the origin of ring structures concentric with large lunar craters. *Physics of the Earth and Planetary Interiors*, *6*(5), 327–339. https://doi.org/10.1016/0031-9201(72)90056-8

Baldwin, R. B. (1981). Tektites: Size estimates of their source craters and implications for their origin. *Icarus*, *45*(3), 554–563. https://doi.org/10.1016/0019-1035(81)90021-X

Bandfield, J. L., Edwards, C. S., Poston, M. J., & Klima, R. L. (2016). Lunar H$_2$O/OH Distributions: Revised Infrared Spectra from Improved Thermal Corrections. Paper presented at the 47th Lunar and Planetary Science Conference, Houston. http://www.lpi.usra.edu/meetings/lpsc2016/pdf/1594.pdf

Bandfield, J. L., Ghent, R. R., Vasavada, A. R., Paige, D. A., Lawrence, S. J., & Robinson, M. S. (2011). Lunar surface rock abundance and regolith fines temperatures derived from LRO Diviner Radiometer data. *Journal of Geophysical Research*, *116*, E00H02. https://doi.org/10.1029/2011je003866

Bandfield, J. L., Hayne, P., Williams, J. P., Greenhagen, B. T., & Paige, D. A. (2015). Lunar surface roughness derived from LRO Diviner Radiometer observations. *Icarus*, *248*, 357–372. https://doi.org/10.1016/j.icarus.2014.11.009

Barker, M. K., Mazarico, E., Neumann, G. A., Zuber, M. T., Haruyama, J., & Smith, D. E. (2016). A new lunar digital elevation model from the Lunar Orbiter Laser Altimeter and SELENE Terrain Camera. *Icarus*, *273*, 346–355. https://doi.org/10.1016/j.icarus.2015.07.039

Basilevsky, A. T., Head, J. W., & Hörz, F. (2013). Survival times of meter-sized boulders on the surface of the Moon. *Planetary and Space Science*, *89*, 118–126. https://doi.org/10.1016/j.pss.2013.07.011

Bray, V. J., Tornabene, L. L., Keszthelyi, L. P., McEwen, A. S., Hawke, B. R., Giguere, T. A., et al. (2010). New insight into lunar impact melt mobility from the LRO camera. *Geophysical Research Letters*, *37*, L21202. https://doi.org/10.1029/2010gl044666

Chin, G., Brylow, S., Foote, M., Garvin, J., Kasper, J., Keller, J., et al. (2007). Lunar Reconnaissance Orbiter overview: The instrument suite and mission. *Space Science Reviews*, *129*(4), 391–419. https://doi.org/10.1007/s11214-007-9153-y

Cintala, M. J., Wood, C. A., & Head, J. W. (1977). The effects of target characteristics on fresh crater morphology: Preliminary results for the Moon and Mercury. In *Lunar and Planetary Science Conference Proceedings* (Vol. 8, pp. 3409–3425).

Cintala, M. J., & Grieve, R. A. F. (1998). Scaling impact-melt and crater dimensions: Implications for the lunar cratering record. *Meteoritics and Planetary Science*, *33*(4), 889–912. https://doi.org/10.1111/j.1945-5100.1998.tb01695.x

Craddock, R. A., & Howard, A. D. (2000). Simulated degradation of lunar impact craters and a new method for age dating farside mare deposits. *Journal of Geophysical Research*, *105*(E8), 20,387–20,401. https://doi.org/10.1029/1999je001099

Dhingra, D., Head, J. W., & Pieters, C. M. (2017). Geological mapping of impact melt deposits at lunar complex craters Jackson and Tycho: Morphologic and topographic diversity and relation to the cratering process. *Icarus*, *283*, 268–281. https://doi.org/10.1016/j.icarus.2016.05.004

Dundas, C. M., Keszthelyi, L. P., Bray, V. J., & McEwen, A. S. (2010). Role of material properties in the cratering record of young platy-ridged lava on Mars. *Geophysical Research Letters*, *37*, L12203. https://doi.org/10.1029/2010gl042869

Fa, W., & Eke, V. R. (2018). Unravelling the mystery of lunar anomalous craters using radar and infrared observations. *Journal of Geophysical Research: Planets*, *123*, 2119–2137. https://doi.org/10.1029/2018JE005668

Fassett, C. I., King, I. R., Nypaver, C. A., & Thomson, B. J. (2018). Temporal evolution of S-Band circular polarization ratios of kilometer-scale craters on the lunar maria. *Journal of Geophysical Research: Planets*, *123*, 3133–3143. https://doi.org/10.1029/2018JE005741

Fassett, C. I., & Thomson, B. J. (2014). Crater degradation on the lunar maria: Topographic diffusion and the rate of erosion on the Moon. *Journal of Geophysical Research: Planets*, *119*, 2255–2271. https://doi.org/10.1002/2014je004698

Florensky, C. P., Basilevsky, A. T., & Grebennik, N. N. (1976). The relationship between lunar crater morphology and crater size. *Moon*, *16*(1), 59–70. https://doi.org/10.1007/BF00648047

Fortezzo, C. M., Spudis, P. D., & Harrel, S. L. (2020). Release of the digital unified global geologic map of the Moon at 1:5,000,000-scale. Paper presented at the 51st Lunar and Planetary Science Conference, Houston. http://www.lpi.usra.edu/meetings/lpsc2020/pdf/2760.pdf

Ghent, R. R., Carter, L. M., Bandfield, J. L., Udovicic, C. J. T., & Campbell, B. A. (2016). Lunar crater ejecta: Physical properties revealed by radar and thermal infrared observations. *Icarus*, *273*, 182–195. https://doi.org/10.1016/j.icarus.2015.12.014

Ghent, R. R., Hayne, P. O., Bandfield, J. L., Campbell, B. A., Allen, C. C., Carter, L. M., & Paige, D. A. (2014). Constraints on the recent rate of lunar ejecta breakdown and implications for crater ages. *Geology*, *42*(12), 1059–1062. https://doi.org/10.1130/G35926.1

Grier, J. A., McEwen, A. S., Lucey, P. G., Milazzo, M., & Strom, R. G. (2001). Optical maturity of ejecta from large rayed lunar craters. *Journal of Geophysical Research*, *106*(E12), 32,847–32,862. https://doi.org/10.1029/1999je001160

Grieve, R. A. F. (1987). Terrestrial impact structures. *Annual Review of Earth and Planetary Sciences*, *15*(1), 245–270. https://doi.org/10.1146/annurev.ea.15.050187.001333

Guo, D. J., Liu, J. Z., Head, J. W., & Kreslavsky, M. A. (2018). Lunar orientale impact basin secondary craters: Spatial distribution, size-frequency distribution, and estimation of fragment size. *Journal of Geophysical Research: Planets*, *123*, 1344–1367. https://doi.org/10.1029/2017je005446

Guo, D., Liu, J., Zhang, F., Sun, Y., Ji, J., Liu, J., et al. (2016). A lunar time scale from geodynamic evolution perspective. Paper presented at the 47th Lunar and Planetary Science Conference, Houston. http://www.hou.usra.edu/meetings/lpsc2016/pdf/1744.pdf

Guo, L., Ji, J. Z., Liu, J. W., Wang, Q. L., & Ouyang, Z. Y. (2016). Preliminary study on the global geotectonic framework of the Moon. *Chinese Journal of Geophysics* Chinese Edition, *59*, 3543–3554. https://doi.org/10.6038/cjg20161002

Haber, J. T., Hayne, P. O., & Elder, C. M. (2018). Rock abundance and surface ages in the lunar maria. Paper presented at the 49th Lunar and Planetary Science Conference, Houston. http://www.lpi.usra.edu/meetings/lpsc2018/pdf/2463.pdf

Hackman, R. J. (1962). Geologic map and sections of the Kepler region of the moon (355). Retrieved from http://pubs.er.usgs.gov/publication/i355

Hale, W., & Head, J. W. (1979). Central peaks in lunar craters: Morphology and morphometry. Paper presented at the Tenth Lunar and Planetary Science Conference, Houston. http://www.lpi.usra.edu/meetings/lpsc1979/pdf/1174.pdf

Hartmann, W. K. (2003). Megaregolith evolution and cratering cataclysm models—Lunar cataclysm as a misconception (28 years later). *Meteoritics & Planetary Science*, *38*(4), 579–593. https://doi.org/10.1111/j.1945-5100.2003.tb00028.x

Hawke, B. R., Blewett, D. T., Lucey, P. G., Smith, G. A., Bell, J. F. III, Campbell, B. A., & Robinson, M. S. (2004). The origin of lunar crater rays. *Icarus*, *170*(1), 1–16. https://doi.org/10.1016/j.icarus.2004.02.013

Hawke, B. R., Giguere, T. A., Gaddis, L. R., Campbell, B. A., Blewett, D. T., Boyce, J. M., et al. (2008). The origin of Copernicus rays: Implications for the calibration of the lunar stratigraphic column. Paper presented at the 39th Lunar and Planetary Science Conference, Houston. https://ui.adsabs.harvard.edu/abs/2008LPI....39.1092H

Head, J. W. (1975). Processes of lunar crater degradation: Changes in style with geologic time. *Moon*, *12*(3), 299–329. https://doi.org/10.1007/Bf02629699

Head, J. W., & Wilson, L. (1992). Lunar mare volcanism: Stratigraphy, eruption conditions, and the evolution of secondary crusts. *Geochimica et Cosmochimica Acta*, *56*(6), 2155–2175. https://doi.org/10.1016/0016-7037(92)90183-j

Heiken, G. H., Vaniman, D. T., & French, B. M. (1991). *Lunar sourcebook: A user's guide to the Moon* (pp. 287–356). New York: Cambridge University Press.

Helfenstein, P., & Shepard, M. K. (1999). Submillimeter-scale topography of the lunar regolith. *Icarus*, *141*(1), 107–131. https://doi.org/10.1006/icar.1999.6160

Hiesinger, H., Head, J. W., Wolf, U., Jaumann, R., & Neukum, G. (2003). Ages and stratigraphy of mare basalts in Oceanus Procellarum, Mare Nubium, Mare Cognitum, and Mare Insularum. *Journal of Geophysical Research*, *108*(E7), 5065. https://doi.org/10.1029/2002je001985

Hiesinger, H., Head, J. W. III, Wolf, U., Jaumann, R., & Neukum, G. (2011). Ages and stratigraphy of lunar mare basalts: A synthesis. In W. A. Ambrose, & D. A. Williams (Eds.), *Recent Advances and Current Research Issues in Lunar Stratigraphy* (Vol. 477, pp. 477–528). Washington, DC: Geological Society of America. https://doi.org/10.1130/2011.2477(01)

Jolliff, B. L., Gillis, J. J., Haskin, L. A., Korotev, R. L., & Wieczorek, M. A. (2000). Major lunar crustal terranes: Surface expressions and crust-mantle origins. *Journal of Geophysical Research*, *105*(E2), 4197–4216. https://doi.org/10.1029/1999JE001103

Jones, E., Caprarelli, G., & Osinski, G. R. (2016). Insights into complex layered ejecta emplacement and subsurface stratigraphy in Chryse Planitia, Mars, through an analysis of THEMIS brightness temperature data. *Journal of Geophysical Research: Planets*, *121*, 986–1015. https://doi.org/10.1002/2015je004879

Kalynn, J., Johnson, C. L., Osinski, G. R., & Barnouin, O. (2013). Topographic characterization of lunar complex craters. *Geophysical Research Letters*, *40*, 38–42. https://doi.org/10.1029/2012gl053608

Kokelaar, B., Bahia, R., Joy, K., Viroulet, S., & Gray, J. (2017). Granular avalanches on the Moon: Mass-wasting conditions, processes, and features. *Journal of Geophysical Research: Planets*, *122*, 1893–1925. https://doi.org/10.1002/2017JE005320

Kreslavsky, M. A., & Head, J. W. (2016). The steepest slopes on the Moon from Lunar Orbiter Laser Altimeter (LOLA) data: Spatial distribution and correlation with geologic features. *Icarus*, *273*, 329–336. https://doi.org/10.1016/j.icarus.2016.02.036

Kreslavsky, M. A., Head, J. W., Neumann, G. A., Rosenburg, M. A., Aharonson, O., Smith, D. E., & Zuber, M. T. (2013). Lunar topographic roughness maps from Lunar Orbiter Laser Altimeter (LOLA) data: Scale dependence and correlation with geologic features and units. *Icarus*, *226*(1), 52–66. https://doi.org/10.1016/j.icarus.2013.04.027

Krüger, T., Hergarten, S., & Kenkmann, T. (2018). Deriving morphometric parameters and the simple-to-complex transition diameter from a high-resolution, global database of fresh lunar impact craters ($D \geq \sim 3$ km). *Journal of Geophysical Research: Planets*, *123*, 2667–2690. https://doi.org/10.1029/2018je005545

Le Feuvre, M., & Wieczorek, M. A. (2011). Nonuniform cratering of the Moon and a revised crater chronology of the inner solar system. *Icarus*, *214*(1), 1–20. https://doi.org/10.1016/j.icarus.2011.03.010

Lemelin, M., Lucey, P. G., Song, E., & Taylor, G. J. (2015). Lunar central peak mineralogy and iron content using the Kaguya Multiband Imager: Reassessment of the compositional structure of the lunar crust. *Journal of Geophysical Research: Planets*, *120*, 869–887. https://doi.org/10.1002/2014je004778

Liu, J., & Guo, D. (2018). Lunar Geological Timescale. In B. Cudnik (Ed.), *Encyclopedia of Lunar Science*. Cham: Springer. https://doi.org/10.1007/978-3-319-05546-6_63-1

Liu, J., & Ji, J. (2018). Lunar Terrane Tectonics. In B. Cudnik (Ed.), *Encyclopedia of Lunar Science*. Cham: Springer. https://doi.org/10.1007/978-3-319-05546-6_62-1

Liu, J. Z., Guo, D. J., Chen, S. B., Sun, Y., Chen, J. P., Wang, X., et al. (2016). Chinese 1:2.5 M geologic mapping of the global Moon. Paper presented at the 47th Lunar and Planetary Science Conference, Houston. http://www.hou.usra.edu/meetings/lpsc2016/pdf/2039.pdf

Liu, J. Z., Ji, J. Z., Zhang, L., Head, J. W., Guo, D. J., Wang, J. T., et al. (2017). New geologic map of the LQ-19 (Mare Nubium) quadrangle on the Moon. Paper presented at the 48th Lunar and Planetary Science Conference, Houston. http://www.hou.usra.edu/meetings/lpsc2017/pdf/1447.pdf

Losiak, A., Wilhelms, D. E., Byrne, C. J., Thaisen, K., Weider, S. Z., Kohout, T., et al. (2009). A new lunar impact crater database. Paper presented at the 40th Lunar and Planetary Science Conference, Houston. https://www.lpi.usra.edu/meetings/lpsc2009/pdf/1532.pdf

Lucchitta, B. K. (1978). Geologic map of the north side of the Moon (1062). Retrieved from http://pubs.er.usgs.gov/publication/i1062

Luther, R., Artemieva, N., & Wunnemann, K. (2019). The effect of atmospheric interaction on impact ejecta dynamics and deposition. *Icarus*, *333*, 71–86. https://doi.org/10.1016/j.icarus.2019.05.007

Luther, R., Zhu, M. H., Collins, G., & Wunnemann, K. (2018). Effect of target properties and impact velocity on ejection dynamics and ejecta deposition. *Meteoritics & Planetary Science*, *53*(8), 1705–1732. https://doi.org/10.1111/maps.13143

Mahanti, P., Robinson, M. S., Thompson, T. J., & Henriksen, M. R. (2018). Small lunar craters at the Apollo 16 and 17 landing sites—Morphology and degradation. *Icarus*, *299*, 475–501. https://doi.org/10.1016/j.icarus.2017.08.018

Mazrouei, S., Ghent, R. R., Bottke, W. F., Parker, A. H., & Gernon, T. M. (2019). Earth and Moon impact flux increased at the end of the Paleozoic. *Science*, *363*(6424), 253–257. https://doi.org/10.1126/science.aar4058

McCauley, J. F., & Wilhelms, D. E. (1971). Geological provinces of the near side of the Moon. *Icarus*, *15*(3), 363–367. https://doi.org/10.1016/0019-1035(71)90114-x

McEwen, A. S., Gaddis, L. R., Neukum, G., Hoffman, H., Pieters, C. M., & Head, J. W. (1993). Galileo observations of post-imbrium lunar craters during the first Earth-Moon flyby. *Journal of Geophysical Research*, *98*(E9), 17,207–17,231. https://doi.org/10.1029/93je01137

Melosh, H. J. (1983). The physics of impact ejecta fragmentation and the origin of meteorites. *Meteoritics*, *18*, 355.

Melosh, H. J. (1989). Impact cratering: A geologic process. In *Oxford Monographs on Geology and Geophysics* (pp. 60–184). New York: Oxford University Press.

Melosh, H. J., & Ivanov, B. A. (1999). Impact crater collapse. *Annual Review of Earth and Planetary Sciences*, *27*(1), 385–415. https://doi.org/10.1146/annurev.earth.27.1.385

Meyer, H. M., Denevi, B. W., Robinson, M. S., & Boyd, A. K. (2020). The global distribution of lunar light plains from the Lunar Reconnaissance Orbiter Camera. *Journal of Geophysical Research: Planets*, *125*, e2019JE006073. https://doi.org/10.1029/2019JE006073

Moriarty Iii, D. P., & Pieters, C. M. (2018). The character of South Pole-Aitken basin: Patterns of surface and subsurface composition. *Journal of Geophysical Research: Planets*, *123*, 729–747. https://doi.org/10.1002/2017JE005364

Mustard, J. F., & Head, J. W. (1996). Buried stratigraphic relationships along the southwestern shores of Oceanus Procellarum: Implications for early lunar volcanism. *Journal of Geophysical Research*, *101*(E8), 18,913–18,925. https://doi.org/10.1029/96JE01826

Nakamura, Y., Latham, G. V., & Dorman, H. J. (1982). Apollo lunar seismic experiment—Final summary. *Journal of Geophysical Research*, *87*(S01), A117. https://doi.org/10.1029/JB087iS01p0A117

Nelson, D. M., Koeber, S. D., Daud, K., Robinson, M. S., Watters, T. R., Banks, M. E., & Williams, N. R. (2014). Mapping lunar maria extents and lobate scarps using LROC image products. Paper presented at the 45th Lunar and Planetary Science Conference, Houston. http://www.lpi.usra.edu/meetings/lpsc2014/pdf/2861.pdf

Neukum, G., Ivanov, B. A., & Hartmann, W. K. (2001). Cratering records in the inner solar system in relation to the lunar reference system. *Space Science Reviews*, *96*(1/4), 55–86. https://doi.org/10.1023/A:1011989004263

Neumann, G. A., Zuber, M. T., Wieczorek, M. A., Head, J. W., Baker, D. M. H., Solomon, S. C., et al. (2015). Lunar impact basins revealed by Gravity Recovery and Interior Laboratory measurements. *Science Advances*, *1*, e1500852. https://doi.org/10.1126/sciadv.1500852

O'Keefe, J. D., & Ahrens, T. J. (1999). Complex craters: Relationship of stratigraphy and rings to impact conditions. *Journal of Geophysical Research*, *104*(E11), 27,091–27,104. https://doi.org/10.1029/1998JE000596

Osinski, G. R., Silber, E. A., Clayton, J., Grieve, R. A. F., Hansen, K., Johnson, C. L., et al. (2019). Transitional impact craters on the Moon: Insight into the effect of target lithology on the impact cratering process. *Meteoritics & Planetary Science*, *54*, 573–591. https://doi.org/10.1111/maps.13226

Paige, D. A., Foote, M. C., Greenhagen, B. T., Schofield, J. T., Calcutt, S., Vasavada, A. R., et al. (2010). The Lunar Reconnaissance Orbiter Diviner lunar radiometer experiment. *Space Science Reviews*, *150*, 125–160. https://doi.org/10.1007/s11214-009-9529-2

Pike, R. J. (1977a). Apparent depth/diameter relation for lunar craters. Paper presented at 8th Lunar and Planetary Science Conference Proceedings.

Pike, R. J. (1977b). Size-dependence in the shape of fresh impact craters on the Moon. Paper presented at Impact and Explosion Cratering: Planetary and Terrestrial Implications.

Richardson, J. E. (2009). Cratering saturation and equilibrium: A new model looks at an old problem. *Icarus*, *204*(2), 697–715. https://doi.org/10.1016/j.icarus.2009.07.029

Robbins, S. J. (2019). A new global database of lunar impact craters >1–2 km: 1. Crater locations and sizes, comparisons with published databases, and global analysis. *Journal of Geophysical Research: Planets*, *124*, 871–892. https://doi.org/10.1029/2018JE005592

Robinson, M. S., Brylow, S. M., Tschimmel, M., Humm, D., Lawrence, S. J., Thomas, P. C., et al. (2010). Lunar Reconnaissance Orbiter Camera (LROC) instrument overview. *Space Science Reviews*, *150*(1–4), 81–124. https://doi.org/10.1007/s11214-010-9634-2

Rosenburg, M. A., Aharonson, O., Head, J. W., Kreslavsky, M. A., Mazarico, E., Neumann, G. A., et al. (2011). Global surface slopes and roughness of the Moon from the Lunar Orbiter Laser Altimeter. *Journal of Geophysical Research*, *116*, E02001. https://doi.org/10.1029/2010je003716

Scott, D. H. (1972). Geologic map of the Eudoxus Quadrangle of the Moon (705). Retrieved from http://pubs.er.usgs.gov/publication/i705

Scott, D. H., Mccauley, J. F., & West, M. N. (1977). Geologic map of the west side of the Moon (1034). Retrieved from http://pubs.er.usgs.gov/publication/i1034

Senthil Kumar, P., Keerthi, V., Senthil Kumar, A., Mustard, J., Gopala Krishna, B., Amitabh, B., et al. (2013). Gullies and landslides on the Moon: Evidence for dry-granular flows. *Journal of Geophysical Research: Planets*, *118*, 206–223. https://doi.org/10.1002/jgre.20043

Senthil Kumar, P., Sruthi, U., Krishna, N., Lakshmi, K. J. P., Menon, R., Amitabh, B., et al. (2016). Recent shallow moonquake and impact-triggered boulder falls on the Moon: New insights from the Schrödinger basin. *Journal of Geophysical Research: Planets*, *121*, 147–179. https://doi.org/10.1002/2015JE004850

Shepard, M. K., Campbell, B. A., Bulmer, M. H., Farr, T. G., Gaddis, L. R., & Plaut, J. J. (2001). The roughness of natural terrain: A planetary and remote sensing perspective. *Journal of Geophysical Research*, *106*(E12), 32,777–32,795. https://doi.org/10.1029/2000je001429

Shkuratov, Y., Kaydash, V., Korokhin, V., Velikodsky, Y., Opanasenko, N., & Videen, G. (2011). Optical measurements of the Moon as a tool to study its surface. *Planetary and Space Science*, *59*(13), 1326–1371. https://doi.org/10.1016/j.pss.2011.06.011

Shkuratov, Y., Kaydash, V., & Videen, G. (2012). The lunar crater Giordano Bruno as seen with optical roughness imagery. *Icarus*, *218*(1), 525–533. https://doi.org/10.1016/j.icarus.2011.12.023

Short, N. M., & Forman, M. L. (1972). Thickness of impact crater ejecta on the lunar surface. *Modern Geology*, *3*, 69–91.

Smith, D. E., Zuber, M. T., Jackson, G. B., Cavanaugh, J. F., Neumann, G. A., Riris, H., et al. (2009). The Lunar Orbiter Laser Altimeter Investigation on the Lunar Reconnaissance Orbiter mission. *Space Science Reviews*, *150*(1–4), 209–241. https://doi.org/10.1007/s11214-009-9512-y

Smith, D. E., Zuber, M. T., Neumann, G. A., Lemoine, F. G., Mazarico, E., Torrence, M. H., et al. (2010). Initial observations from the Lunar Orbiter Laser Altimeter (LOLA). *Geophysical Research Letters*, *37*, L18204. https://doi.org/10.1029/2010gl043751

Stöffler, D., Ryder, G., Ivanov, B. A., Artemieva, N. A., Cintala, M. J., & Grieve, R. A. F. (2006). Cratering history and lunar chronology. *Reviews in Mineralogy and Geochemistry*, *60*(1), 519–596. https://doi.org/10.2138/rmg.2006.60.05

Vaughan, W. M., & Head, J. W. (2014). Impact melt differentiation in the South Pole-Aitken basin: Some observations and speculations. *Planetary and Space Science*, *91*, 101–106. https://doi.org/10.1016/j.pss.2013.11.010

Watters, T. R., Robinson, M. S., Collins, G. C., Banks, M. E., Daud, K., Williams, N. R., & Selvans, M. M. (2015). Global thrust faulting on the Moon and the influence of tidal stresses. *Geology*, *43*(10), 851–854. http://doi.org/10.1130/G37120.1

Watters, T. R., Weber, R. C., Collins, G. C., Howley, I. J., Schmerr, N. C., & Johnson, C. L. (2019). Shallow seismic activity and young thrust faults on the Moon. *Nature Geoscience*, *12*(6), 411–417. https://doi.org/10.1038/s41561-019-0362-2

Werner, S. C., & Medvedev, S. (2010). The lunar rayed-crater population—Characteristics of the spatial distribution and ray retention. *Earth and Planetary Science Letters*, *295*(1–2), 147–158. https://doi.org/10.1016/j.epsl.2010.03.036

Whitten, J. L., & Head, J. W. (2013). Detecting volcanic resurfacing of heavily cratered terrain: Flooding simulations on the Moon using Lunar Orbiter Laser Altimeter (LOLA) data. *Planetary and Space Science*, *85*, 24–37. https://doi.org/10.1016/j.pss.2013.05.013

Wieczorek, M. A., Neumann, G. A., Nimmo, F., Kiefer, W. S., Taylor, G. J., Melosh, H. J., et al. (2013). The crust of the Moon as seen by GRAIL. *Science*, *339*(6120), 671–675. https://doi.org/10.1126/science.1231530

Wilhelms, D. E. (1970). *Summary of lunar stratigraphy-telescopic observations, Professional Paper 599-F*. Washington DC: US Government Printing Office. https://doi.org/10.3133/pp599F

Wilhelms, D. E., & Byrne, C. J. (2009). Stratigraphy of lunar craters. Retrieved from http://www.imageagain.com/Strata/StratigraphyCraters.2.0.htm

Wilhelms, D. E., & El-Baz, F. (1977). Geologic map of the east side of the Moon (948). Retrieved from http://pubs.er.usgs.gov/publication/i948

Wilhelms, D. E., McCauley, J. F., & Trask, N. J. (1987). *The geologic history of the Moon, USGS Professional Paper 1348* (pp. 1–281). Washington DC: US Government Printing Office. https://doi.org/10.3133/pp1348

Wood, C., Head, J., & Cintala, M. (1977). Crater degradation on mercury and the moon: Clues to surface evolution. Paper presented at 8th Lunar and Planetary Science Conference Proceedings.